HIGH-ORDER ACCURATE CONSERVATIVE FINITE DIFFERENCE METHODS FOR VLASOV EQUATIONS IN 2D+2V[*]

JEFFREY W. BANKS[†], ANDRE GIANESINI ODU[†], RICHARD BERGER[‡],
THOMAS CHAPMAN[‡], WILLIAM ARRIGHI[‡], AND STEPHAN BRUNNER[§]

Abstract. This manuscript discusses discretization of the Vlasov–Poisson system in 2D+2V phase space using high-order accurate conservative finite difference algorithms. One challenge confronting direct kinetic simulation is the significant computational cost associated with the high-dimensional phase space description. In the present work we advocate the use of high-order accurate schemes as a mechanism to reduce the computational cost required to deliver a given level of error in the computed solution. We pursue a discretely conservative finite difference formulation of the governing equations, and discuss fourth- and sixth-order accurate schemes. In addition, we employ a minimally dissipative nonlinear scheme based on the well-known WENO (weighted essentially nonoscillatory) approach. Verification of the full formulation is performed using the method of manufactured solutions. Results are also presented for the physically relevant scenarios of Landau damping, and growth of transverse instabilities from an imposed plane wave.

Key words. Vlasov simulation, conservative finite differences, high-order accuracy

AMS subject classifications. 65M06, 65M12, 65M20

DOI. 10.1137/19M1238551

1. Introduction. The field of plasma physics has a large number of applications for which so-called kinetic effects, i.e., the (nonlinear) interaction of particles with their associated plasma waves, are of critical importance. For example, wakefield acceleration of electron beams by nonlinear wave-particle interaction is being pursued as part of an effort to generate TeV energies for linear colliders for high-energy-physics applications [22, 39, 37], or MeV energies with application to medical and other technologies [60, 31]. Other nonlinear wave interactions, such as backward Raman scattering [38] and backward Brillouin scattering [58], are being studied with the aim of producing light wave intensities and laser pulse compression beyond what is achievable using current chirped pulse amplification [41, 54]. Less intense laser-driven nonlinear wave-particle interactions play a role in inertial confinement fusion (ICF) for facilities such as the National Ignition Facility (NIF), where parametric instabilities such as stimulated Brillouin scattering, stimulated Raman scattering, and two-plasmon decay may have a deleterious impact on experiments. In contrast to accelerator applications, ICF experiments seek to keep these instabilities below a threshold for growth, although there has been limited success in accomplishing this goal as the energy and power required for ignition reach more than the 500 TW and

[†]Rensselaer Polytechnic Institute, 110 8th Street, Troy, NY 12180 (banksj3@rpi.edu, gianea@rpi.edu).

[‡]Lawrence Livermore National Laboratory, P.O. Box 808, Livermore, CA 94551 (berger5@llnl.gov, chapman29@llnl.gov, arrighi2@llnl.gov).

[§]Ecole Polytechnique Fédérale de Lausanne (EPFL), CH-1015 Lausanne, Switzerland (stephan.brunner@epfl.ch).

2 MJ available at the NIF. Since the most promising results to date for high neutron yield at the NIF have used shorter pulses at the highest laser power (and therefore intensity) available, large and nonlinear plasma waves with significant kinetic effects may be unavoidable. In summary, understanding kinetic dynamics in plasmas is an important and long-standing problem in basic physics, and computational simulation has long been at the center of this effort.

Historically, the predominant tool for simulating kinetic effects has been particle-in-cell methods. Here the motion of some number of charged particles, N_p, through a physical domain, is coupled to a description of the self-consistent electromagnetic fields. This approach has the conceptual advantage that there are in fact a finite number of particles in any physical system, and so if N_p is taken large enough the underlying physical problem of interest can be treated directly. Unfortunately, the number of charged particles in the physical system is typically many orders of magnitude too large for direct simulation on even the largest computers. The typical approach is to draw a particular sample, in a statistical sense, from an underlying distribution of particles. However, for a given random draw with practically realizable N_p, the statistical variation is typically much larger than the physical thermal fluctuations, and so studying physical instabilities that grow from thermal noise is challenging. From an algorithmic perspective, one may wish to consider the limit $N_p \to \infty$. This limit leads to the Klimontovich equation [44], and by taking an ensemble average of many such instances one arrives at the well-known Vlasov equation,

$$(1.1) \quad \partial_t f(\mathbf{x}, \mathbf{v}, t) + \mathbf{v} \cdot \nabla_{\mathbf{x}} f(\mathbf{x}, \mathbf{v}, t) + \frac{q}{m} \left(\mathbf{E}(\mathbf{x}, t) + \mathbf{v} \times \mathbf{B}(\mathbf{x}, t) \right) \cdot \nabla_{\mathbf{v}} f(\mathbf{x}, \mathbf{v}, t) = 0,$$

describing the evolution of a probability density function (PDF) f in so-called phase space consisting of d spatial and d velocity dimensions.[1] In (1.1) $\mathbf{x} \in \mathcal{R}^d$ are the physical space coordinates, $\mathbf{v} \in \mathcal{R}^d$ are the d-components of velocity, t is time, q is the particle charge, m is the particle mass, $\mathbf{E}$ is the electric field, and $\mathbf{B}$ is the magnetic field. For three-dimensional simulations, $d = 3$ and so the phase space is fully six dimensional. However, in practice, computations with smaller d, e.g., $d = 2$, are often pursued.

This continuum description of the evolution of a PDF is inherently free from statistical noise, and is therefore well-suited for detailed studies of kinetic instabilities. However, the price is the need for direct representation of the PDF in a full six dimensional phase space $(\mathbf{x}, \mathbf{v})$. This is a heavy cost, and with the exception of a few isolated instances, Vlasov systems are typically simulated in a reduced-dimensionality phase space or utilizing a spherical harmonic decomposition of velocity space. For example, in the classical work of Cheng and Knorr [16], numerical approximation of solutions to the Vlasov–Poisson system in one physical and one velocity dimension, so-called 1D+1V, were sought using a semi-Lagrangian technique. Since that time, research into numerical methods for Vlasov systems has blossomed, and the set of discretization tools includes semi-Lagrangian [43, 42, 24], pseudo-spectral [26, 51, 52], finite element [10, 17], finite volume [2, 23, 53, 7, 56], and finite difference [32, 21, 12] methods. However, despite significant advances, the cost of full 3D-3V computations remains prohibitive, and the current state-of-the art appears to be 2D-2V, e.g., [4, 8, 51, 52]. Underscoring the significant burden of cost for kinetic simulation, one obvious trend in recent years is a push toward highly efficient and high-order accurate methods. It

---

[1]Note that in (1.1) the notation $\partial_t f$ indicates partial differentiation with respect to time. Similar notation will be adopted for other coordinate directions.

is well known that high-order methods often obtain more accurate answers with fewer degrees of freedom than their low-order counterparts. However, the aforementioned 2D-2V studies place direct emphasis on computational efficiency even within a given class of high-order accurate approximations. The present work will continue this emphasis and describe high-order accurate finite difference algorithms with the potential for significant improvements in cost with respect to their finite volume predecessors. In addition, we note that despite the trend toward high efficiency and high-order accuracy, the published literature contains very few reports of quantifiable verification of Vlasov codes (e.g., [13]), nor of the enabling capabilities of high-order schemes versus their low-order counterparts. These will both be a focus of the present work.

The present manuscript discusses recent algorithmic developments and code verification specifically targeted to high-dimensional continuum kinetic simulation. The overarching approach is to reduce the cost of phase-space computation and, thereby, enable simulation of a wide class of kinetic problems, e.g., those in plasma physics as addressed in this work. The algorithms which we describe are implemented in the LOKI code, which solves 2D+2V-Vlasov systems of single or multiple species using high-order accurate algorithms. Originally formulated using fourth-order accurate finite volumes [7], LOKI was successfully used to study a variety of physical instabilities including electron-plasma wave (EPW) wavefront bowing [4], EPW self-focusing [59], and EPW filamentation [8]. Motivated by increasingly complex applications and therefore increased computational burden, LOKI was then reformulated to use conservative finite differences (FD) in order to reduce overall computational cost. These fourth-order accurate conservative FD algorithms were successfully applied to problems of the effect of pitch angle collisions on EPW damping [5], and 2D+2V ion acoustic wave (IAW) instability [15], but they were unfortunately not described in any documentation or published manuscript. The present work both remedies this oversight, and describes extension of the approach to sixth-order accuracy with the aim of further reducing the cost of kinetic simulation as necessitated by more complex problems of plasma physics. The fourth- and sixth-order accurate conservative FD schemes will be described in section 3. The accuracy of the algorithms, and their implementation in LOKI , are then investigated in section 4. Section 4.1 gives code verification results using the method of manufactured solutions and demonstrates convergence at the expected rate. Section 4.2 then presents results for the classical problem of collisionless (Landau) damping, again with an emphasis on demonstration of expected convergence rates. Finally, in section 4.3 we compare the computational cost savings of the sixth- versus fourth-order accurate schemes when applied to the study of IAW instability. Concluding remarks are then given in section 5.

2. Governing equations. In order to focus on the spatial and temporal discretization of the Vlasov equation, consider the physical scenario of a collisionless and electrostatic plasma in periodic physical domain $x \in [-L_x, L_x]$, $y \in [-L_y, L_y]$. In addition, we adopt the dimensional reduction to $d = 2$ and consider the 2D+2V Vlasov–Poisson system

$$(2.1a) \qquad \partial_t f_s + \partial_x (v_x f_s) + \partial_y (v_y f_s) + \frac{q_s}{m_s} \left[\partial_{v_x} (E_x f_s) + \partial_{v_y} (E_y f_s) \right] = 0,$$

$$(2.1b) \qquad E_x = -\partial_x \phi, \qquad E_y = -\partial_y \phi,$$

$$(2.1c) \qquad \partial_x^2 \phi + \partial_y^2 \phi = -\rho,$$

$$(2.1d) \qquad \rho = \sum_s \rho_s, \qquad \rho_s = q_s \int_{-\infty}^{\infty} \int_{-\infty}^{\infty} f_s \, dv_x \, dv_y.$$

Here the subscripts s are used to indicate the constituent species (e.g., $s = e$ for electron, $s = i$ for ion), ρ is the total charge density, ρ_s are the charge density contributions from species s, ϕ is the electrical potential, $[x, y]^T$ are the two components of configuration space, and $[v_x, v_y]^T$ are the two components of velocity with $v_x \in (-\infty, \infty)$, $v_y \in (-\infty, \infty)$. Note that the functional dependence of the arguments in (2.1), e.g., $f(x, y, v_x, v_y, t)$, have been suppressed for brevity. Note also that the Vlasov equation (2.1a) has been expressed in conservative form, since v_x, v_y, E_x, and E_y are independent of the respective differentiation directions and therefore are free to pass through the derivative operators.

The Vlasov system (2.1) describes the evolution of the distribution functions for some number of charge species under the effect of their self-consistent electrostatic fields. In general, the species present in the plasma will depend on the underlying matter and its ionization state. In addition, simplifying assumptions may be appropriate in some cases. Therefore to simplify the presentation in the remainder of this manuscript, we consider two canonical cases which are selected for their relevance to EPW, and IAW dynamics, respectively.

Electron plasma: As the name suggests, for EPWs the primary dynamic of interest is the evolution of the electrons. The reason for this is that the dynamical time scale of interest is short in comparison to the time required to accelerate the heavy ions. It is therefore justified to take $m_i/m_e \to \infty$, and consider a single Vlasov equation for the electrons with $s = e$ while the ion distribution function is assumed to be time independent and, in our cases, spatially uniform as $f_i = f_M(v_x, v_y; \eta_i)$, where f_M is a standard normalized Maxwellian distribution

$$(2.2) \qquad f_M(v_x, v_y; \eta) \equiv \frac{\eta^2}{2\pi} e^{-\frac{1}{2}\eta^2(v_x{}^2 + v_y{}^2)}.$$

In general, the parameter η is related to the temperature, but the value of η_i is immaterial for the case of an electron plasma.

Two-species plasma: For IAWs, the dynamics of both electrons and ions are important. In the present manuscript we consider the canonical case of a two-species plasma with $m_i/m_e = 1836$ corresponding to hydrogen, as well as reduced mass scenarios with $m_i/m_e = 1$ and $m_i/m_e = 10$. In all cases, the species indicator s is either i for ions or e for electrons.

3. Discretization of the Vlasov–Poisson system. Discretization of the governing Vlasov–Poisson system presented in section 2 involves a number of ingredients. These include the discretization of the derivatives in the Vlasov equations, the discretization of the Poisson equation, derivation of fields from the potential, computation of charge densities (including truncation of velocity to a finite domain), and time integration. In this work, the discretization of the Vlasov equation uses unique minimally diffusive nonlinear conservative FD schemes, as will be discussed in section 3.1. All other spatial derivatives, in particular those associated with the derivation of the electric fields, use standard high-order accurate centered differences, and the integrals involved in the computation of charge densities use a standard composite quadrature; see section 3.2. Time integration via a method-of-lines formulation and Runge–Kutta time stepping is discussed briefly in section 3.3. Finally, a brief overview of the parallelization strategy employed in LOKI is discussed in 3.4.

Before discussing the details of the discretization, let us introduce some notation. In the FD discretizations used in this work, the unknown quantities are given on cell-centered grids in a four-dimensional (4-D) phase space or a two-dimensional

(2-D) physical (configuration) space. For example, in the x-direction for the domain $x \in [x_a, x_b]$, the grid points are given as $x_{i_x} = x_a + (i_x + \frac{1}{2})h_x$ for $i_x = 0, \ldots, N_x$ and grid spacing $h_x = (x_b - x_a)/N_x$. Additional ghost cells (n_g at each boundary) are used for the imposition of boundary conditions. For fourth-order accuracy $n_g = 2$, while for sixth-order accuracy $n_g = 3$. Additional specifics of the discrete boundary conditions will be discussed below. Discrete grid functions will be indicated using subscripts; in particular, $\mathbf{i} = (i_x, i_y)$ indicates a spatial grid index, while $\mathbf{j} = (j_{v_x}, j_{v_y})$ indicates a velocity grid index. This notation explicitly indicates the dimensionality of a particular discrete grid function. For example, the grid function for a distribution function is a time-dependent 4D object $f_{s,\mathbf{i},\mathbf{j}} \approx f_s(x_{i_x}, y_{i_y}, v_{x_{j_{v_x}}}, v_{y_{j_{v_y}}}, t)$, where the time dependence is omitted for simplicity. Similarly, the density is a time-dependent 2D object $\rho_{\mathbf{i}} \approx \rho(x_{i_x}, y_{i_y}, t)$. The grids are assumed to have N_x, N_y, $N_{vx,s}$, and $N_{vy,s}$ points in the x-, y-, v_x-, v_y-directions, respectively. Note that the velocity grids may be species dependent, but there is a single physical-space grid.

In this work, the discrete truncation of the infinite domain is considered a modeling choice, and its accuracy is contingent on the fact that distribution functions necessarily decay as $\|\mathbf{v}\| \to \infty$. As a result, one simply uses finite minimum and maximum velocities for each dimension so that the magnitude of the distribution function near these large velocity boundaries is sufficiently small. In particular, by taking the maximum velocity to be 7 times the species thermal velocity, the Maxwellian distribution would have decayed to $\approx 10^{-12}$. For distribution functions which deviate from Maxwellian, larger thermal maxima may be needed to retain the same threshold, and in practice one should monitor the distribution at the artificial high-velocity boundaries to ensure that the distribution function remains small. In general the maximum velocity depends on the species, and the direction, but for simplicity we will take the maximum and minimum bounds to be symmetric in each coordinate direction as in $-v_{x,\min,s} = v_{x,\max,s}$, and $-v_{y,\min,s} = v_{y,\max,s}$. With the velocity boundaries truncated, the density moment reduction in (2.1d) becomes

$$(3.1) \qquad \rho_s \approx q_s \int_{-v_{x,\min,s}}^{v_{x,\max,s}} \int_{-v_{y,\min,s}}^{v_{y,\max,s}} f_s \, dv_x \, dv_y.$$

At the artificially truncated velocity boundaries, a characteristic condition is implemented which samples the background distribution at inflow, and then subsequently extrapolates to the ghost cells. For example, at the $v_{x,\max}$ boundary, the first stage is to override the distribution function on the boundary if the x-acceleration is negative, i.e.,

$$f_{s,\mathbf{i},j_{N_{vx}},j_{v_y}} \leftarrow f_M(v_{x_{j_{N_{vx}}}}, v_{y_{j_{v_y}}}) \qquad \text{if} \qquad q_s E_{x\mathbf{i}} < 0.$$

The distribution function is then extrapolated to the ghost cells by fitting a fourth-order polynomial for the fourth-order accurate scheme, or by fitting a sixth-order polynomial for the sixth-order accurate scheme. The other velocity boundaries are treated similarly

As discussed in section 2, periodicity in both the x- and y-directions is assumed. For the cell-centered grid used here, this is implemented, for example, by setting

$$f_{s,-i_g,i_y,\mathbf{j}} = f_{s,N_x+1-i_g,i_y,\mathbf{j}} \qquad \text{for} \qquad i_g = 1, \ldots, n_g.$$

All other physical boundaries are treated similarly.

3.1. FD discretization for the Vlasov equations. As discussed in [7], the minimum spatial scales present in Vlasov simulation tend to become smaller as time

increases, due primarily to the natural filamentation and possible development of phase-space turbulence. As a result, sub-grid-scale features inevitably arise in long-time simulation, which, in combination with nonlinearity of the equations, can lead to numerical difficulties. To alleviate these difficulties, a particular numerical flux was derived. This numerical flux was based on ideas drawn from weighted essentially nonoscillatory (WENO) [30, 49, 50] and uses upwinding to incorporate numerical dissipation. However, the new scheme was derived specifically to minimize added dissipation so that well-resolved solutions will use the centered dissipation free scheme. This new minimally diffusive flux was called BWENO, short for "Banks" WENO, and we shall adopt this nomenclature here. The BWENO flux was then used in a finite volume discretization, as discussed, for example, in [20] or [14].

The current work is built around the BWENO flux, but reformulates the basic discretization using high-order accurate conservative FDs. Both fourth- and sixth-order accurate discretizations are pursued in this work. The primary motivation to reformulate as an FD scheme is that, particularly at high order and in high dimensions, the computational cost is significantly reduced in comparison to the finite volume (FV) formulation. Prior work discussing the cost of FV is discussed for example in [14]. In the present work, sixth-order discretizations of the 4D Vlasov equation are considered, and the potential savings of an FD formulation are particularly significant. In this case, because the FV stencil is "thick," i.e., the stencil fills out in all coordinate directions, the sixth-order 7-pt stencil has $\sim 7^4 = 2401$ grid points. In contrast, the FD stencil remains "thin," i.e., uses only grid points along the coordinate direction, and therefore has only $\sim 7 \times 4 = 28$ stencil points. All other things being equal, this is a factor of ~ 85 times less work for the FD reformulation. Additional motivation for the reformulation includes simplifying the addition of external source terms (i.e., in the FD framework only pointwise evaluations of a forcing function are needed while in the FV framework cell average evaluation is required), as are used in this work with manufactured solutions for code verification.

The formulation of the conservative FD schemes that are used here is generic. For clarity of presentation it is therefore advantageous to focus on the derivative in a generic direction, here called the ξ-direction, and suppress all notation relating to the other directions. It is understood that all derivatives in the Vlasov equation (2.1a) are then treated similarly. To ensure that the approximation is discretely conservative, we begin with the ansatz that the derivative at a particular grid point ξ_j is exactly represented as a difference of fluxes, i.e.,

$$(3.2) \qquad \partial_\xi u_j = D_{+\xi} \hat{u}_{j-1/2} = \frac{\hat{u}_{j+1/2} - \hat{u}_{j-1/2}}{\Delta \xi},$$

where $u(\xi)$ is an arbitrary smooth function, $\hat{u}(\xi)$ is a flux function whose form must be determined so that (3.2) is exact, and the subscript notation is used to imply restriction to the grid, e.g., $u_j = u(\xi_j)$. Note that we will later use the subscript notation to indicate a discrete grid function. Note also that we adopt the standard notation for divided difference operators, $D_{\pm\xi}$ and $D_{0\xi}$, whose action is defined as

$$D_{+\xi} q_j \stackrel{\text{def}}{=} \frac{q_{j+1} - q_j}{\Delta \xi}, \quad D_{-\xi} q_j \stackrel{\text{def}}{=} \frac{q_j - q_{j-1}}{\Delta \xi}, \quad D_{0\xi} q_j \stackrel{\text{def}}{=} \frac{q_{j+1} - q_{j-1}}{2\Delta \xi}.$$

Following the approach in [6, 1], the flux, $\hat{u}$, can be found by seeking an expansion of the form

$$(3.3) \qquad \hat{u}_{j-1/2} = \left[\sum_{m=0}^{\infty} \alpha_m (\Delta \xi \partial_\xi)^{2m} \right] u_{j-1/2}.$$

Using this ansatz and enforcing that (3.2) be exact for smooth functions (i.e., using $u = \exp(ik\xi)$ for wave number k) then implies the transcendental equation

$$\frac{\zeta}{2} - \sin\left(\frac{\zeta}{2}\right) \sum_{m=0}^{\infty} \alpha_m (-\zeta^2)^m = 0,$$

where $\zeta = k\Delta\xi$ is the so-called grid wave number. Taylor expansion for small ζ leads to an infinite triangular system for the α_m coefficients, the first 4 or which are $\alpha_0 = 1$, $\alpha_1 = -\frac{1}{24}$, $\alpha_2 = \frac{7}{5760}$, and $\alpha_3 = -\frac{31}{967680}$. Truncation of the expansion to a finite number of terms, and replacing the continuous derivatives in (3.3) with discrete approximations then leads to a form of numerical flux and, ultimately, a discretely conservative and accurate approximation for the derivative.

Building on the basis of conservative FD schemes, the fundamental idea behind the BWENO flux, as discussed in [7], is to use a nonlinear combination of low-order fluxes where the relative weighting yields a centered flux for well-resolved solutions, but an upwind flux in regions of sharp gradients. In particular, the scheme uses a flux of the form

(3.4) $$\hat{u}_{j-1/2}^{(p,B)} = w_{j-1/2}^{(p-1,L)} \hat{u}_{j-1/2}^{(p-1,L)} + w_{j-1/2}^{(p-1,R)} \hat{u}_{j-1/2}^{(p-1,R)},$$

where $\hat{u}_{j-1/2}^{(p,B)}$ indicates the pth order BWENO flux, $\hat{u}_{j-1/2}^{(p-1,\Xi)}$ for $\Xi = L, R$ are left and right biased fluxes of order $p-1$, while $w_{j-1/2}^{(p-1,\Xi)}$ are the weights applied to the fluxes. The biased fluxes $\hat{u}_{j-1/2}^{(p-1,\Xi)}$ are constructed in the framework of (3.3) using a $(p-1)$-point stencil which is biased one point to the left or right. Specific examples for fourth and sixth order are given in sections 3.1.1 and 3.1.2, respectively. The definition of the weights follows the discussion in [7], and the formulation draws heavily from the WENO literature [30, 49]. In particular, as in [49], minimizing the total variation of the biased polynomial interpolants of u lead to smoothness indicators β,

$$\beta_{j-1/2}^{(p-1,\Xi)} = \sum_{m=1}^{p-1} \int_{\xi_{j-1}}^{\xi_j} \Delta\xi^{2m-1} (\partial_\xi^m \tilde{u}^{(p-1,\Xi)}(\xi))^2 \, d\xi,$$

where $\tilde{u}^{(p-1,\Xi)}$, for $\Xi = L, R$ are the left and right biased polynomial interpolants of u. As in WENO, weights associated with the left and right interpolants are then defined as

$$\tilde{w}_{j-1/2}^{(p-1,\Xi)} = \frac{a_{j-1/2}^{(p-1,\Xi)}}{a_{j-1/2}^{(p-1,L)} + a_{j-1/2}^{(p-1,R)}},$$

$$a_{j-1/2}^{(p-1\Xi)} = \frac{d}{\epsilon + \beta_{j-1/2}^{(p-1,\Xi)}},$$

where $d = 1/2$ are the ideal weights, and ϵ is a small parameter to avoid division by zero (taken to be $\epsilon = 10^{-10}$ in the code). Optional mapping steps for the interpolant weights $\tilde{w}$ can be performed as suggested by Henrick, Aslam, and Powers [27]. The default in LOKI is one mapping step. The BWENO weights are then defined to apply the larger of the two stencil weights to the upwind direction, independently of smoothess. Thus, assuming the local advection velocity is given as v, this last step is

given by

$$
\left.
\begin{aligned}
w_{j-1/2}^{(p-1,L)} &= \max\left(\tilde{w}_{j-1/2}^{(p-1,L)}, \tilde{w}_{j-1/2}^{(p-1,R)}\right) \\
w_{j-1/2}^{(p-1,R)} &= \min\left(\tilde{w}_{j-1/2}^{(p-1,L)}, \tilde{w}_{j-1/2}^{(p-1,R)}\right)
\end{aligned}
\right\} \quad \text{if } v > 0,
$$

$$
\left.
\begin{aligned}
w_{j-1/2}^{(p-1,L)} &= \min\left(\tilde{w}_{j-1/2}^{(p-1,L)}, \tilde{w}_{j-1/2}^{(p-1,R)}\right) \\
w_{j-1/2}^{(p-1,R)} &= \max\left(\tilde{w}_{j-1/2}^{(p-1,L)}, \tilde{w}_{j-1/2}^{(p-1,R)}\right)
\end{aligned}
\right\} \quad \text{else.}
$$

One important aspect of the schemes construction is that in the limit of well-resolved solutions, the weights are designed to approach the ideal weight $d = 1/2$, and the BWENO flux is designed to fall back to the centered flux of order p, indicated as $\hat{u}_{j-1/2}^{(p,C)}$. This is an intentional design goal, and the general pth order BWENO schemes have the property that, for well-represented solutions, the pth-order centered FD approximation is used. However, the scheme introduces numerical dissipation when solution features cannot be represented on a given mesh. The nature of the equations being solved is that smooth initial conditions remain smooth for all time since characteristics cannot cross in phase space. As a result, there is not a possibility of self-steepening discontinuities, i.e., shocks, and so adequate viscosity is provided by the $(p-1)$-order upwind approximation. The result is a scheme which allows for a smooth, solution-dependent transition between the pth order central flux and the $(p-1)$-order upwind flux, while retaining a fixed $(p+1)$-point stencil. Furthermore, since smooth initial conditions remain smooth for all time, sufficiently fine grids essentially yeild the pth-order accurate, dissipation free, centered scheme.[2]

3.1.1. Fourth-order BWENO. It is useful to present the mechanics of this process using the example of fourth-order accuracy since the extensions to higher order follow directly. Therefore, consider a fourth-order conservative FD approximation, which is obtained by retaining 2 terms in (3.3) to give

$$(3.5) \qquad \hat{u}_{j-1/2}^{(4)} = u_{j-1/2} - \frac{\Delta\xi^2}{24}\partial_\xi^2 u_{j-1/2} = \hat{u}_{j-1/2} + O(\Delta\xi^4),$$

where the superscript (4) indicates the order of accuracy. To obtain fourth-order accuracy, discretization of the continuous terms in the 4-pt stencil surrounding the point $\xi_{j-1/2}$ uses

$$u_{j-1/2} = \frac{1}{16}\left(-u_{j+1} + 9u_j + 9u_{j-1} - u_{j-2}\right) + O(\Delta\xi^4),$$

$$\partial_\xi^2 u_{j-1/2} = \frac{1}{2\Delta\xi^2}\left(u_{j+1} - u_j - u_{j-1} + u_{j-2}\right) + O(\Delta\xi^2).$$

Substituting back into the flux (3.5) then yields

$$\hat{u}_{j-1/2}^{(4,C)} = \frac{1}{12}\left(-u_{j+1} + 7u_j + 7u_{j-1} - u_{j-2}\right),$$

which in turn leads to the standard fourth-order accurate centered difference scheme

$$\partial_\xi^{(4,C)} u_j = \frac{1}{12\Delta\xi}\left(-u_{j+2} + 8u_{j+1} - 8u_{j-1} + u_{j-2}\right).$$

---

[2] As discussed in Henrick, Aslam, and Powers [27], the convergence rate may degrade at certain types of critical points. This degradation is ameliorated by their proposed mapping, which is why we use it in practice.

To derive the fourth-order BWENO flux, third-order accurate left and right biased flux stencils are needed. The left biased flux is defined using

$$u_{j-1/2} = \frac{1}{8} \left(3u_j + 6u_{j-1} - u_{j-2}\right) + O(\Delta\xi^3),$$

$$\partial_\xi^2 u_{j-1/2} = \frac{1}{\Delta\xi^2} \left(u_j - 2u_{j-1} + u_{j-2}\right) + O(\Delta\xi),$$

and similarly on the right. Substitution into (3.5) then yields the left and right biased fluxes

$$\hat{u}_{j-1/2}^{(3,L)} = \frac{1}{6} \left(2u_j + 5u_{j-1} - u_{j-2}\right),$$

$$\hat{u}_{j-1/2}^{(3,R)} = \frac{1}{6} \left(-u_{j+1} + 5u_j + 2u_{j-1}\right).$$

Note that $\hat{u}_{j-1/2}^{(4,C)} = (\hat{u}_{j-1/2}^{(3,L)} + \hat{u}_{j-1/2}^{(3,R)})/2$. The relative weights for the left and right biased fluxes are then defined using the smoothness indicators β,

$$\beta_{j-1/2}^{(3,L)} = \beta^{(3)}\left(u_{j-1}\right), \qquad \beta_{j-1/2}^{(3,R)} = \beta^{(3)}\left(u_j\right).$$

Here the action of the nonlinear operator $\beta^{(3)}(\cdot)$ on the grid function u_j is as follows:

$$\beta^{(3)}(u_j) = \left(\Delta_2^1 u_j\right)\left(\left(\Delta_2^1 u_j\right) + \left(\Delta_2^2 u_j\right)\right) + \frac{4}{3}\left(\Delta_2^2 u_j\right)^2$$

with $\left(\Delta_p^d u_j\right)$ being the pth-order accurate undivided difference approximation to the dth derivative, specifically,

$$\left(\Delta_2^1 u_j\right) = \frac{1}{2}\left(u_{j+1} - u_{j-1}\right),$$

$$\left(\Delta_2^2 u_j\right) = u_{j+1} - 2u_j + u_{j-1}.$$

3.1.2. Sixth-order BWENO. The mechanics of deriving the sixth-order accurate scheme follow directly from the fourth-order accurate case. In particular, retaining 3 terms in (3.3) gives

$$\hat{u}_{j-1/2}^{(6)} = u_{j-1/2} - \frac{\Delta\xi^2}{24}\partial_\xi^2 u_{j-1/2} + \frac{7\Delta\xi^4}{5760}\partial_\xi^4 u_{j-1/2} = \hat{u}_{j-1/2} + O(\Delta\xi^6),$$

which after discretizing in a 6-pt stencil surrounding the point $\xi_{j-1/2}$ yields the sixth-order centered flux

$$\hat{u}_{j-1/2}^{(6,C)} = \frac{1}{60}\left(u_{j+2} - 8u_{j+1} + 37u_j + 37u_{j-1} - 8u_{j-2} + u_{j-3}\right).$$

As before, the left and right biased fluxes are found by using biased 5-pt stencils which leads to

$$\hat{u}_{j-1/2}^{(5,L)} = \frac{1}{60}\left(-3u_{j+1} + 27u_j + 47u_{j-1} - 13u_{j-2} + 2u_{j-3}\right),$$

$$\hat{u}_{j-1/2}^{(5,R)} = \frac{1}{60}\left(2u_{j+2} - 13u_{j+1} + 47u_j + 27u_{j-1} - 3u_{j-2}\right).$$

Last, the smoothness coefficients are found to be

$$\beta_{j-1/2}^{(5,L)} = \beta^{(5)}\left(u_{j-1}\right), \qquad \beta_{j-1/2}^{(5,R)} = \beta^{(5)}\left(u_j\right),$$

where the action of the nonlinear operator $\beta^{(5)}(\cdot)$ on the grid function u_j is as follows:

$$\begin{aligned}
\beta^{(5)}(u_j) = \left(\Delta_4^1 u_j\right) & \left(\left(\Delta_4^1 u_j\right) + \left(\Delta_4^2 u_j\right) + \frac{1}{3}\left(\Delta_2^3 u_j\right) + \frac{1}{12}\left(\Delta_2^4 u_j\right)\right) \\
& + \left(\Delta_4^2 u_j\right)\left(\frac{4}{3}\left(\Delta_4^2 u_j\right) + \frac{5}{4}\left(\Delta_2^3 u_j\right) + \frac{2}{5}\left(\Delta_2^4 u_j\right)\right) \\
& + \left(\Delta_2^3 u_j\right)\left(\frac{83}{60}\left(\Delta_2^3 u_j\right) + \frac{23}{18}\left(\Delta_2^4 u_j\right)\right) \\
& + \frac{437}{315}\left(\Delta_2^4 u_j\right)^2
\end{aligned}$$

and, as before, $\left(\Delta_p^d u_j\right)$ are the pth-order accurate undivided difference approximation to the dth derivative, specifically,

$$\begin{aligned}
\left(\Delta_4^1 u_j\right) &= \frac{1}{12}\left(-u_{j+2} + 8u_{j+1} - 8u_{j-1} + u_{j-2}\right), \\
\left(\Delta_4^2 u_j\right) &= \frac{1}{12}\left(-u_{j+2} + 16u_{j+1} - 30u_j + 16u_{j-1} - u_{j-2}\right), \\
\left(\Delta_2^3 u_j\right) &= \frac{1}{2}\left(u_{j+2} - 2u_{j+1} + 2u_{j-1} - u_{j-2}\right), \\
\left(\Delta_2^4 u_j\right) &= \left(u_{j+2} - 4u_{j+1} + 6u_j - 4u_{j-1} + u_{j-2}\right).
\end{aligned}$$

3.2. Discretizations for electric fields. The derivation of the electric fields from distribution functions requires three basic components: moment reduction to derive charge densities, solution of the Poisson equation to give the electric potential, and derivation of the electric fields from the electric potential. Each of these is briefly discussed below.

3.2.1. Quadratures for moment reductions. The computation of *moments* from distribution functions by integration over velocity space is a common operation in kinetic codes. For example, computation of charge densities, currents, kinetic energy, etc.; all require moment computations. In the present work, the charge density ρ_s is given through such a moment reduction, as expressed in (2.1d) and subsequently on a truncated velocity domain as in (3.1). Given that the velocity domain has been truncated with the assumption that the distribution function is negligible there, we use a midpoint quadrature to approximate the velocity integrals, i.e.,

$$(3.6) \qquad \rho_{s\mathbf{i}} = h_{v_x} h_{v_y} q_s \sum_{j_{v_x}=0}^{N_{vx}} \sum_{j_{v_y}=0}^{N_{vy}} f_{s,\mathbf{i},j_{v_x},j_{v_y}} = h_{v_x} h_{v_y} q_s \sum_{\mathbf{j}} f_{s,\mathbf{i},\mathbf{j}}.$$

As discussed in [34, 55], for example, this class of quadrature schemes is spectrally accurate on periodic data. Given the assumptions of the velocity truncation, the assumption of periodicity holds here to the level of roundoff error. Numerical results in section 4 support this conclusion and there are no signs of errors associated with our treatment of the artificially truncated high-velocity boundaries.

3.2.2. Discretization of Poisson equation for electric potential. With the charge density in hand, standard centered FDs are used to discretize Poisson's equation.[3] Similarly to the numerical treatment of the Vlasov equation discussed in section 3.1, it is convenient to present the approach for an arbitrary direction ξ. However, in contrast to the case of the BWENO scheme for the Vlasov equation, there are no complex algorithmic tools employed here and so it is convenient to seek an exact expression for the derivative in terms of an infinite expansion of difference operators of the form

$$(3.7) \qquad \partial_\xi^2 u_j = \left[\sum_{m=0}^\infty \beta_m \Delta\xi^{2m} (D_{+\xi} D_{-\xi})^{m+1} \right] u_j.$$

The coefficients β are found by insisting that the expansion (3.7) be exact (i.e., using $u = \exp(ikx)$ for wave number k), which yields the equation

$$\left[\sum_{m=0}^\infty \beta_m \left(-4\sin^2 \left(\frac{\zeta}{2} \right) \right)^{m+1} \right] + \zeta^2 = 0.$$

Taylor expansion for small ζ gives an infinite triangular system for the β_m coefficients, the first 4 or which are $\beta_0 = 1$, $\beta_1 = -\frac{1}{12}$, $\beta_2 = \frac{1}{90}$, and $\beta_3 = -\frac{1}{560}$. Truncation of the expansion to a finite number of terms then yields the centered derivatives, which for fourth and sixth order are

$$\left(\partial_\xi^2 \right)^{(4,C)} u_j = \frac{1}{12\Delta\xi^2} \left(-u_{j+2} + 16u_{j+1} - 30u_j + 16u_{j-1} - u_{j-2} \right),$$

$$\left(\partial_\xi^2 \right)^{(6,C)} u_j = \frac{1}{180\Delta\xi^2} \left(2u_{j+3} - 27u_{j+2} + 270u_{j+1} - 490u_j \right.$$
$$\left. + 270u_{j-1} - 27u_{j-2} + 2u_{j-3} \right),$$

where the order of the operator is indicated by the superscript. For example, $(\partial_\xi^2)^{(p,C)}$ indicates the pth-order accurate centered approximation to the second derivative. Note that the qualifier "C" has been included here, although it is not necessary since there are no biased counterparts, simply to be consistent with the notation in the rest of the manuscript.

3.2.3. Derivation of electric fields from potential. Computation of the fields from the electric potential uses the centered discretization of the first derivatives as presented in section 3.1. In particular, the fourth- and sixth-order accurate centered difference approximations for the first derivative are

$$\partial_\xi^{(4,C)} u_j = \frac{1}{12\Delta\xi} \left(-u_{j+2} + 8u_{j+1} - 8u_{j-1} + u_{j-2} \right),$$

$$\partial_\xi^{(6,C)} u_j = \frac{1}{60\Delta\xi} \left(u_{j+3} - 9u_{j+2} + 45u_{j+1} - 45u_{j-1} + 9u_{j-2} - u_{j-3} \right).$$

Note that one can also directly derive the same discrete stencils by considering expansions of the derivative of the form

$$(3.8) \qquad \partial_\xi u_j = \left[D_{0\xi} \sum_{m=0}^\infty \gamma_m \Delta\xi^{2m} (D_{+\xi} D_{-\xi})^m \right] u_j.$$

---

[3]Due to the periodic boundary conditions adopted here, it is also possible to use a spectral discretization based on FFTs. However, we have chosen to use an FD approximation for its convenience and flexibility, e.g., nonperiodic BCs.

Forcing exactness leads to

$$(3.9) \qquad \sin(\zeta) \left[\sum_{m=0}^{\infty} \gamma_m \left(-4\sin^2\left(\frac{\zeta}{2}\right) \right)^m \right] - \zeta = 0,$$

and after expanding for small ζ gives $\gamma_0 = 1$, $\gamma_1 = \frac{1}{6}$, $\gamma_2 = \frac{1}{30}$, $\gamma_3 = -\frac{1}{140}, \ldots$.

3.3. Time stepping. Our approach to time evolution uses a method-of-lines formulation with explicit Runge–Kutta time stepping. All necessary components of the spatial discretization have been presented in the prior sections, and so the semi-discrete system of equations for an order of accuracy p can be expressed as

$$(3.10a) \qquad \begin{aligned} \partial_t f_{s,\mathbf{i},\mathbf{j}} = &-\partial_x^{(p,B)}(v_{x,\mathbf{j}} f_{s,\mathbf{i},\mathbf{j}}) - \partial_y^{(p,B)}(v_{y,\mathbf{j}} f_{s,\mathbf{i},\mathbf{j}}) \\ &- \frac{q_s}{m_s} \left[\partial_{v_x}^{(p,B)}(E_{x,\mathbf{i}} f_{s,\mathbf{i},\mathbf{j}}) + \partial_{v_y}^{(p,B)}(E_{y,\mathbf{i}} f_{s,\mathbf{i},\mathbf{j}}) \right], \end{aligned}$$

$$(3.10b) \qquad E_{x,\mathbf{i}} = -\partial_x^{(p,C)}\phi_{\mathbf{i}}, \qquad E_{y,\mathbf{i}} = \partial_y^{(p,C)}\phi_{\mathbf{i}},$$

$$(3.10c) \qquad \left(\partial_x^2\right)^{(p,C)}\phi_{\mathbf{i}} + \left(\partial_y^2\right)^{(p,C)}\phi_{\mathbf{i}} = -\rho_{\mathbf{i}},$$

$$(3.10d) \qquad \rho_{\mathbf{i}} = \sum_s \rho_{s,\mathbf{i}}, \qquad \rho_{s,\mathbf{i}} = q_s h_{v_x} h_{v_y} \sum_{\mathbf{j}} f_{s,\mathbf{i},\mathbf{j}}.$$

Equation (3.10) is a system of $N_{\text{tot}} = \sum_s N_x N_y N_{vx,s} N_{vy,s}$ ODEs, where we recall that N_x and N_y are the number of grid points in the x- and y-direction in physical space, respectively, and $N_{vx,s}$ and $N_{vy,s}$ are the number of grid points in the v_x- and v_y-direction in velocity space, respectively. The N_{tot} ODEs are time advanced using explicit Runge–Kutta (RK) of the appropriate order. There are many potential RK schemes that could be applied to (3.10), and as is well known for WENO-type schemes, some choices may have subtle consequences; e.g., see [57]. Given the emphasis of the present manuscript on spatial discretizations, we therefore pick fourth- and sixth-order RK schemes whose stability regions contains a portion of the imaginary axis, where the eigenvalues for the Vlasov operator lie. Butcher tableaus for these RK schemes are presented in Figure 1. For aid in interpreting these tables see [3], for example. The associated stability regions are shown in the top panel of Figure 2.

At the beginning of each time step, the time-step size, Δt, is chosen to ensure that the spectra of the continuous operator for the periodic problem, with all Fourier modes supported on the discrete grid, lies within the stability region. Specifically

$$(3.11) \qquad \Delta t = \Lambda C_p \left[\pi \left(\frac{v_{x,\max}}{h_x} + \frac{v_{y,\max}}{h_y} + \frac{a_{x,\max}}{h_{v_x}} + \frac{a_{y,\max}}{h_{v_y}} \right) \right]^{-1},$$

where $v_{x,\max}$ and $v_{y,\max}$ are the maximum coordinate velocities over all species, $a_{x,\max} = \frac{q_s}{m_s}\max_{\mathbf{i}}(|E_{x\mathbf{i}}|)$ and $a_{y,\max} = \frac{q_s}{m_s}\max_{\mathbf{i}}(|E_{y\mathbf{i}}|)$ are the maximum components of the acceleration over all species, C_p is an order-dependent quantity indicating the approximate breadth of the stability region on the imaginary axis, and Λ is a safety factor taken to be close to 1. In this work, for the RK-4 scheme, $C_4 = 2.6$ while for the RK-6 scheme, $C_6 = 3.1$. Note that since the acceleration depends on the fields, which in turn depend on the distribution functions, Δt will in general change at each time step, although for simplicity we have suppressed notation explicitly indicating this. Note also that since the maximum component velocities and accelerations are taken over all species, for multispecies plasmas it is common for the lighter species (e.g., electrons), to dominate the time-step selection.

Left tableau (classical RK-4):

$$
\begin{array}{c|cccc}
0 & & & & \\
\frac{1}{2} & \frac{1}{2} & & & \\
\frac{1}{2} & 0 & \frac{1}{2} & & \\
1 & 0 & 0 & 1 & \\
\hline
 & \frac{1}{6} & \frac{1}{3} & \frac{1}{3} & \frac{1}{6}
\end{array}
$$

Right tableau (sixth-order accurate integrator):

$$
\begin{array}{c|cccccccc}
0 & & & & & & & & \\
\frac{1}{9} & \frac{1}{9} & & & & & & & \\
\frac{1}{6} & \frac{1}{24} & \frac{1}{8} & & & & & & \\
\frac{1}{3} & \frac{1}{6} & -\frac{1}{2} & \frac{2}{3} & & & & & \\
\frac{1}{2} & \frac{935}{2536} & -\frac{2781}{2536} & \frac{309}{317} & \frac{321}{1268} & & & & \\
\frac{2}{3} & -\frac{12710}{951} & \frac{8287}{317} & -\frac{40}{317} & -\frac{6335}{317} & 8 & & & \\
\frac{5}{6} & \frac{5840285}{3104064} & -\frac{7019}{2536} & -\frac{52213}{86224} & \frac{1278709}{517344} & -\frac{433}{2448} & \frac{33}{1088} & & \\
1 & -\frac{5101675}{1767592} & \frac{112077}{25994} & \frac{334875}{441898} & -\frac{973617}{883796} & -\frac{1421}{1394} & \frac{333}{5576} & \frac{36}{41} & \\
\hline
 & \frac{41}{840} & 0 & \frac{9}{35} & \frac{9}{280} & \frac{34}{105} & \frac{9}{280} & \frac{9}{35} & \frac{41}{840}
\end{array}
$$

FIG. 1. *Butcher tableaus defining the explicit RK time integrators used in this work. On the left is the classical RK-4 integrator used for the fourth-order accurate scheme, and on the right is the sixth-order accurate integrator.*

An additional question concerning the time integration is if the BWENO stencils might push the discrete spectra outside the stability region. The bottom left and bottom right frames of Figure 2 address this question by plotting the discrete spectra of the advection operator in 1 dimension with various levels of upwinding. Recall that when $w^L = w^R = 1/2$, the centered scheme is obtained and the eigenvalues of the discrete operator are pure imaginary. However, upwind stencils are applied in underresolved regions, and the eigenvalues are pushed into the left half-plane. In all cases the discrete spectra remain well inside the stability region of the integrator.[4] Note that this analysis corresponds to using the same BWENO weights for the right and left flux, which is certainly not true in practice. In addition, further complications could arise from our discrete treatment of the truncated velocity boundaries. Nevertheless, the analysis suggests stability with chosen RK integrators and for the time step chosen using 3.11, and no instabilities are observed in any computation.

3.4. Parallelization strategy. Even using high-order accurate discretization strategies, practical phase-space computation often leads to systems with very large numbers of degrees of freedom. As a result, parallelization of the algorithms, in order to make use of large compute resources, is usually a necessity. Although detailed descriptions and performance analysis of the parallel algorithms used in the LOKI code is beyond the scope of the present article, it is appropriate to say a few words about the overall parallel strategy we use.

At present, parallel communication is accomplished via the message passing interface (MPI) [25]. The data in the LOKI code are structured into logically rectangular arrays which are either 2D (as in the case of the fields, electric potential, etc.), or 4D (as in the case of distribution functions). In all simulations presented here, the 2D arrays are all assigned to a single MPI rank, $\mathcal{P}_1$ say. Here, a direct LU-factorization of

---

[4]The plots in Figure 2 indicate that the time step could be chosen larger than suggested by (3.11), perhaps by as much as a factor of 2. These larger time steps have not been considered in this work.
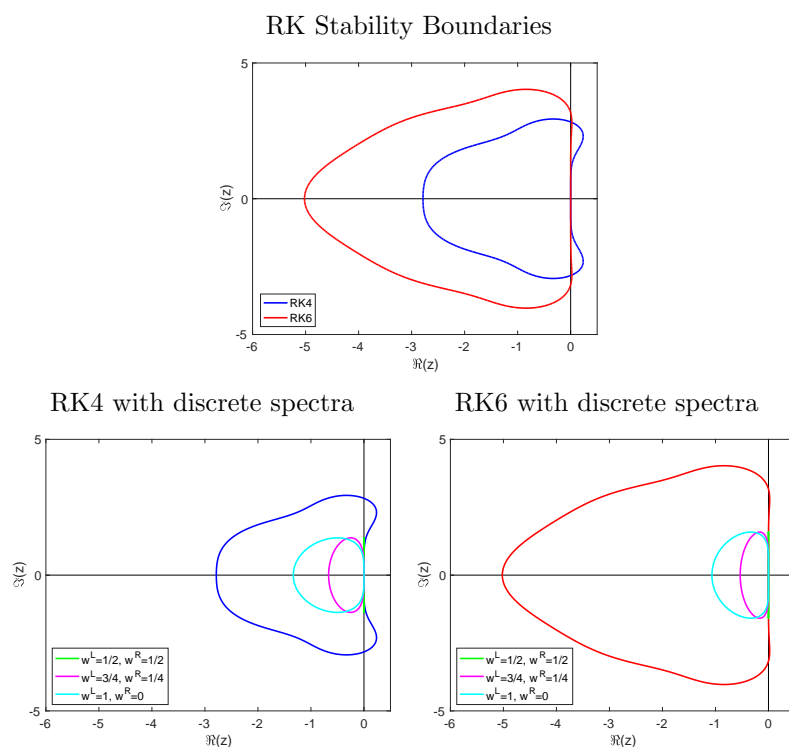
FIG. 2. *On the top center are the stability regions (and simplified stability bounds) for the RK methods defined by the Butcher tableaus in Figure* 1. *On the bottom left are the bounds for fourth order, along with the discrete spectra for the BWENO-4 stencils with various amounts of upwinding as defined by flux stencil weights w^L and w^R. On the bottom right are the bounds for sixth order, along with the discrete spectra for the BWENO-6 stencils with various amounts of upwinding as defined by flux stencil weights w^L and w^R.*

the matrix associated with the Poisson equation for the electric potential is performed at program start up, and the solution of the Poisson equation for the electric potential is then accomplished via back substitution. The 4D arrays for the kinetic species are then distributed across the remainder of the MPI ranks, and for this purpose the P++ parallel array class is used [47], with each species α being assigned to the set of MPI ranks denoted $\mathcal{P}_\alpha$.

Using this parallel data layout, the time-stepping algorithm is arranged in a manner designed to minimize potential wasted CPU cycles by overlapping communication and computation in a multiple-instruction multiple-data paradigm. The algorithm proceeds as follows. First, the moment reduction to compute the charge density $\rho_{\mathbf{i}}$ in (3.10d) is performed locally on each MPI rank in $\mathcal{P}_\alpha$. The local densities are then reduced to the single MPI rank $\mathcal{P}_1$. At this point, $\mathcal{P}_1$ is tasked with computing the electric fields and communicating the result back to $\mathcal{P}_\alpha$ when this computation is complete. Before the electric field has been received by $\mathcal{P}_\alpha$, those ranks are tasked with computing the spatial streaming derivatives $\partial_x^{(p,B)}(v_{x,\mathbf{j}}f_{s,\mathbf{i},\mathbf{j}})$ and $\partial_y^{(p,B)}(v_{y,\mathbf{j}}f_{s,\mathbf{i},\mathbf{j}})$. Once the computation of the streaming derivatives has been completed, the electric fields will have been received by all $\mathcal{P}_\alpha$, and the remaining derivatives to complete the right-hand side of (3.10a) can be calculated.

4. Numerical results. Having described the full numerical discretization in section 3, we now move on to a series of numerical results. The simulation results which are presented have the goals of verifying the accuracy of the approach, as well as illustrating the benefits of our high-order accurate treatment in physically meaningful scenarios. For the purposes of verification, manufactured solutions are first employed, followed by convergence estimates for the physically motivated problems of Landau damping in EPWs and IAWs. The latter tests are a segue into a more complex example studying IAW instability in 2D+2V. By comparing to prior results from the literature (obtained using the fourth-order accurate formulation), this case illustrates the significant computational savings that can be attained by moving from fourth- to sixth-order accuracy.

4.1. Method of manufactured solutions. The method of manufactured solutions (MMS), a term coined by Roache in [48], but previously called twilight zone [18, 11, 28], is a powerful tool for code verification. The fundamental idea underlying MMS is to add forcing functions to the governing equations. The forcing is chosen so that a given (known) function is an exact solution to the governing equations with added forcing. Following this basic prescription, one can choose exact solutions with sufficient smoothness to verify the expected convergence properties of the discrete operator. Importantly, this procedure is applicable to equations with significant non-linearities or other complications that preclude the construction of exact solutions to the unforced equations.

In general, the application of MMS requires forcing to be included in all components of the governing equations, e.g., boundary conditions, constraint equations, etc. However, solutions to the governing Vlasov system (2.1) have certain features that have been exploited in the discretization. For example, solutions decay exponentially as $|\mathbf{v}| \to \infty$ and so the infinite domain is truncated to a finite domain to give (3.1). Furthermore, from a practical perspective it is unwieldy to specify independent exact solutions for all dependent quantities in (2.1) (such as f_s, E_x, ρ_s, etc.), which would, in general, necessitate forcing functions to be added to all equations. Instead, we pursue an approach that requires forcing only in the Vlasov equation (2.1a). That is to say that, for a given system of exact particle distribution functions $f_s^{(e)}(\mathbf{x}, \mathbf{v}, t)$, the corresponding electric fields (including charge density, electric potential, and the fields themselves) are computed analytically, as implied by the unforced (2.1b)–(2.1d). This eliminates the need to independently force the equations associated with the derivation of the electric fields, and leaves only the choice of the exact distribution functions $f_s^{(e)}(\mathbf{x}, \mathbf{v}, t)$. Because many problems of physical interest involve perturbations of Maxwellian distribution functions, which are steady states of the Vlasov system (2.1), it is natural to use spatial and temporal perturbations of normalized Maxwellian distributions as the manufactured exact solution. In particular, consider exact solutions of the form

$$(4.1) \qquad f_s^{(e)}(x, y, v_x, v_y, t) = f_M(v_x, v_y; \eta_s) \left[1 + \delta\rho_s(x, y, t)\right],$$

where $\delta\rho_s$ is a known function. Since all solutions are assumed spatially periodic on a box of size $2L_x \times 2L_y$, we take

$$\delta\rho_s(x, y, t) = A_s \cos(k_x x) \cos(k_y y) \sin(k_t t)$$

for k_x and k_y integers, and A_s an amplitude with $|A_s| < 1$ to avoid negative PDFs. Note that positive manufactured solutions are not strictly required by the mathematics, or indeed the numerical implementation, but negative distributions are unphysical

and so we choose to avoid them. Note also that in general one could allow $\delta\rho_s$ to be a function of $\mathbf{v}$, although the full $f_s^{(e)}$ is already a nontrivial function of $\mathbf{v}$, and so this would not bring any essential changes to the process.

Electron plasma: In the case of an electron plasma, the ion mass is assumed to be large in comparison to the electron mass (i.e., the mass ratio is taken to be $m_i/m_e \to \infty$), and the ions are therefore considered to be a stationary neutralizing background. This is equivalent to considering an ion distribution function of the form $f_i = f_M(v_x, v_y; \eta_i)$, where the value of η_i is immaterial since the ion distribution is uniform in space and time, and the definition of the Maxwellian in (2.2) is normalized so that the velocity integral is 1. As a result, only the dynamics of the electrons are computed, where the electron mass is $m_e = 1$, the electron charge is $q_e = -1$, and $\eta_e = 1$. Using the definition of $f_e^{(e)}$ from (4.1), the charge density is

$$(4.2) \qquad \rho^{(e)}(x, y, t) = 1 - \delta\rho_e(x, y, t),$$

and so the average charge density over the domain vanishes:

$$\int_{\mathbf{\Omega}} \rho^{(e)}(\mathbf{x}, t) d\mathbf{x} = 0.$$

In this case, the electric potential and fields are, therefore,

$$(4.3) \quad \phi^{(e)} = \frac{-A_e c_x c_y s_t}{\left(k_x^2 + k_y^2\right)}, \qquad E_x^{(e)} = \frac{-A_e k_x s_x c_y s_t}{\left(k_x^2 + k_y^2\right)}, \qquad E_y^{(e)} = \frac{-A_e k_y c_x s_y s_t}{\left(k_x^2 + k_y^2\right)},$$

where the notation has the meaning $c_x = \cos(k_x x)$, $c_y = \cos(k_y y)$, $s_x = \sin(k_x x)$, $s_y = \sin(k_y y)$, $s_t = \sin(k_t t)$, and $c_t = \cos(k_t t)$. To complete the definition of the manufactured solution source term for the Vlasov system for an electron plasma one also requires the following derivatives of the exact solution $f_s^{(e)}$:

$$(4.4a) \qquad \partial_t f_e^{(e)} = f_M(v_x, v_y; 1) A_e k_t c_x c_y c_t,$$

$$(4.4b) \qquad \partial_x f_e^{(e)} = -f_M(v_x, v_y; 1) A_e k_x s_x c_y s_t,$$

$$(4.4c) \qquad \partial_y f_e^{(e)} = -f_M(v_x, v_y; 1) A_e k_y c_x s_y s_t,$$

$$(4.4d) \qquad \partial_{v_x} f_e^{(e)} = -v_x f_M(v_x, v_y; 1) \left(1 - A_e c_x c_y s_t\right),$$

$$(4.4e) \qquad \partial_{v_y} f_e^{(e)} = -v_y f_M(v_x, v_y; 1) \left(1 - A_e c_x c_y s_t\right).$$

Finally, the manufactured solution source term for an electron plasma, here called h, is added to the the right-hand side of (2.1a) so that the modified system becomes

$$(4.5a) \qquad \partial_t f_s + \partial_x(v_x f_s) + \partial_y(v_y f_s) + \frac{q_s}{m_s}\left[\partial_{v_x}(E_x f_s) + \partial_{v_y}(E_y f_s)\right] = h,$$

$$(4.5b) \qquad h = \partial_t f_e^{(e)} + v_x \partial_x f_e^{(e)} + v_y \partial_x f_e^{(e)} - E_x^{(e)} \partial_{v_x} f_e^{(e)} - E_x^{(e)} \partial_{v_x} f_e^{(e)}.$$

Using this manufactured solution with $A_s = 0.1$, $L_x = 2\pi$, $L_y = \pi$, $k_x = 4$, $k_y = 4$, and $k_t = 1$, convergence studies are performed for both the fourth- and sixth-order accurate methods. In all cases the artificial velocity boundaries are defined using $v_{x,\max} = 7$, $v_{y,\max} = 9$, computations are run to a final time of $t_f = 1.0$ with $\Lambda = 1$, and results are presented for both L_∞ and discrete L_2-norms. Simulations are performed at 16 different grid resolutions defined using $N_x = N_y = N_{vx} = N_{vy} = \lceil 1.2^k N_0 \rceil$ for
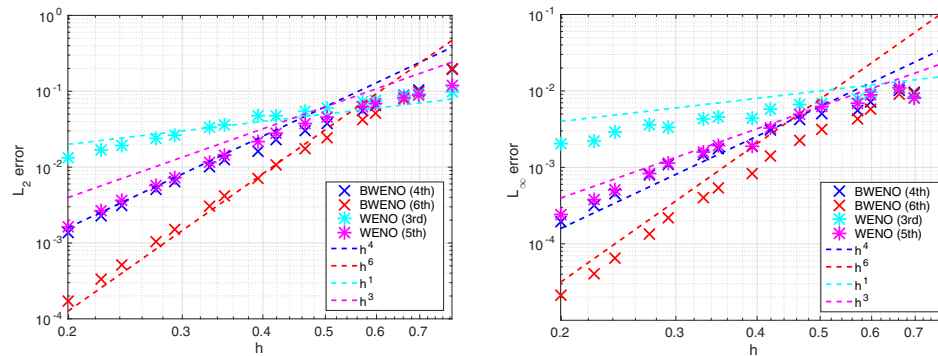
FIG. 3. *Single species L_2- (left) and L_∞- (right) norm convergence results for the manufactured solution. Results are presented for the fourth- and sixth-order accurate schemes using blue and red colored "x" marks, respectively, and reference lines indicating $\mathcal{O}(h^4)$ and $\mathcal{O}(h^6)$ are also included. The designed order of accuracy of the two schemes is apparent.*

$k \in [0,7]$ and $N_0 = 16, 18$, and the results are presented in Figure 3. In addition, for comparison purposes in this case, the figure presents results from the classical WENO-3 scheme with our RK-4 time stepping and the WENO-5 scheme with our RK-6 time stepping. These WENO schemes are implemented as discussed in [49], and are chosen since the maximum extent of their discrete stencils corresponds to BWENO-4 and BWENO-6 stencils, respectively. In these studies, the domains and grids are chosen so that the grid spacing in each direction is different, which we have found to be useful for the purposes of debugging. In the figure, it is clear that both BWENO schemes are converging at, or near, their designed order-of-accuracy in both L_∞ and L_2. On the other hand, the classical WENO schemes both exhibit degraded convergence rates, which is a well-known phenomenon for WENO schemes applied to solutions with local extrema [27]. Note also that the BWENO-6 scheme shows an advantage over BWENO-4 in that fewer grid points are required to reach a given error. Requiring fewer grid points for a given error is the primary motivator for moving to higher-order schemes, particularly for the present case in a 4D phase space, and so this behavior is expected.

Because the observed convergence rates for the errors in both L_∞ and L_2 are consistent with each other, no localized behavior in the error is expected. However, given the 4D nature of the phase space solution, one must apply some kind of dimensional reduction to visualize the result. Here we take the approach of moment reduction of the error into the 2D physical space (x, y), which is equivalent to considering the error in the charge density. Figure 4 compares errors in the charge density for the sixth-order scheme at low ($N_x = 18$) and high ($N_x = 63$) resolutions.[5] For the $N_x = 18$ the spatial resolution is arguably insufficient to resolve the variation, but there are nevertheless no obvious artifacts attributable to the nonlinear BWENO stencil selection. For $N_x = 64$, the simulation is quite well resolved, and the error is quite smooth throughout physical space.

Two-species plasma: In the case of mobile ions, the mass ratio is taken to be finite. Therefore, the dynamics of both the ions and electrons are evolved. Using the

------

[5]Results for the fourth-order scheme showing qualitatively similar behavior are not shown for brevity.
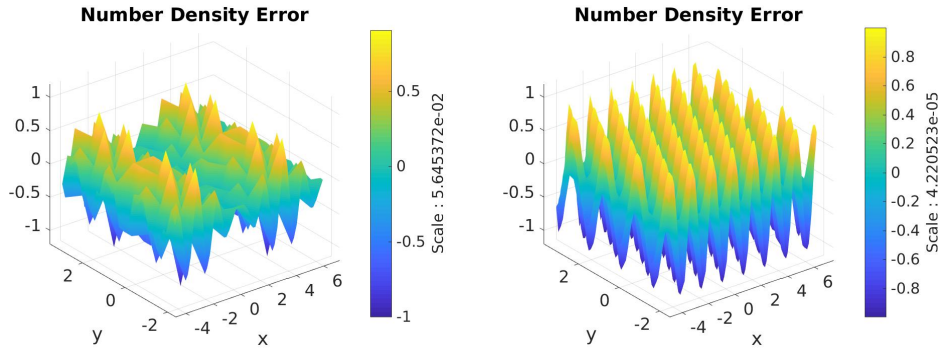
Fig. 4. *Error in number density for the single species manufactured solution at sixth-order accuracy. On the left are results using* 18 *grid points per dimension, while on the right are results using* 63 *grid points per dimension. Note that the color scale for each figure has been normalized as indicated to the right of each color bar.*

definition of $f_s{}^{(e)}$ from (4.1), the charge density is therefore

$$(4.6) \qquad \rho(x, y, t) = \delta f_i(x, y, t) - \delta f_e(x, y, t),$$

where $\int_{\boldsymbol{\Omega}} \rho(\mathbf{x}, t) d\mathbf{x} = 0$. Thus the electric potential and fields are

$$(4.7) \qquad \phi = \sum_s \frac{-A_s c_{x,s} c_{y,s} s_{t,s}}{\left(k_{x,s}^2 + k_{y,s}^2\right)}, \qquad E_x = \sum_s \frac{-A_s k_{x,s} s_{x,s} c_{y,s} s_{t,s}}{\left(k_{x,s}^2 + k_{y,s}^2\right)},$$
$$E_y = \sum_s \frac{-A_s k_{y,s} c_{x,s} s_{y,s} s_{t,s}}{\left(k_{x,s}^2 + k_{y,s}^2\right)},$$

where the notation once again has the meaning $c_{x,s} = \cos(k_{x,s}x)$, $c_{y,s} = \cos(k_{y,s}y)$, $s_{x,s} = \sin(k_{x,s}x)$, $s_{y,s} = \sin(k_{y,s}y)$, and $s_{t,s} = \sin(k_{t,s}t)$.

Simulations are performed for three different plasmas with increasing density ratios. Generally the case of lighter ions corresponds to an easier test numerically since the time-scale separation between electron and ion dynamics grows with the mass ratio, but the case of light ions is less physically relevant. The largest density ratio used here corresponds to a hydrogen plasma. In all cases, $m_e = 1$, $q_e = -1$, $\eta_e = 1$, while for the ion species $m_i = 1, 10, 1836$, $q_i = 1$, and $\eta_i = \sqrt{m_i}$. In this case, the maximum velocity for each species is scaled by η_s in order to account for the decreasing width of the equilibrium distribution as η_s increases. Therefore, $v_{max,x,s} = 7/\eta_s$, $v_{max,y,s} = 9/\eta_s$. The manufactured solutions use $A_e = 0.1$, $A_i = 0.2$, $L_x = 2\pi$, $L_y = \pi$, $k_{x,i} = 2$, $k_{x,e} = 4$, $k_{y,i} = 4$, $k_{y,e} = 2$, and $k_{t,i} = k_{t,e} = 1$. Convergence studies are performed at a final time $t_f = 4.0$ with $\Lambda = 1$ for both the fourth- and sixth-order accurate schemes, and errors are computed using both the discrete L_2- and the L_∞-norms. The results of the convergence study using grids defined by $N_x = N_y = N_{vx} = N_{vy} = \lceil 1.2^k N_0 \rceil$, for $k \in [0, 7]$ and $N_0 = 16, 18$ are presented in Figure 5. In all cases the designed order of accuracy is clearly demonstrated. It is worthwhile to notice that the L_∞-error for the ions tends to increase as the ion mass is increased since the maximum of the ion distribution function is also increasing. On the other hand, the L_2-error for the ions remains relatively constant since the effect of the increasing maximum in the distribution is offset by the decreasing width in velocity space, as required to maintain the normalization of the Maxwellian. As in
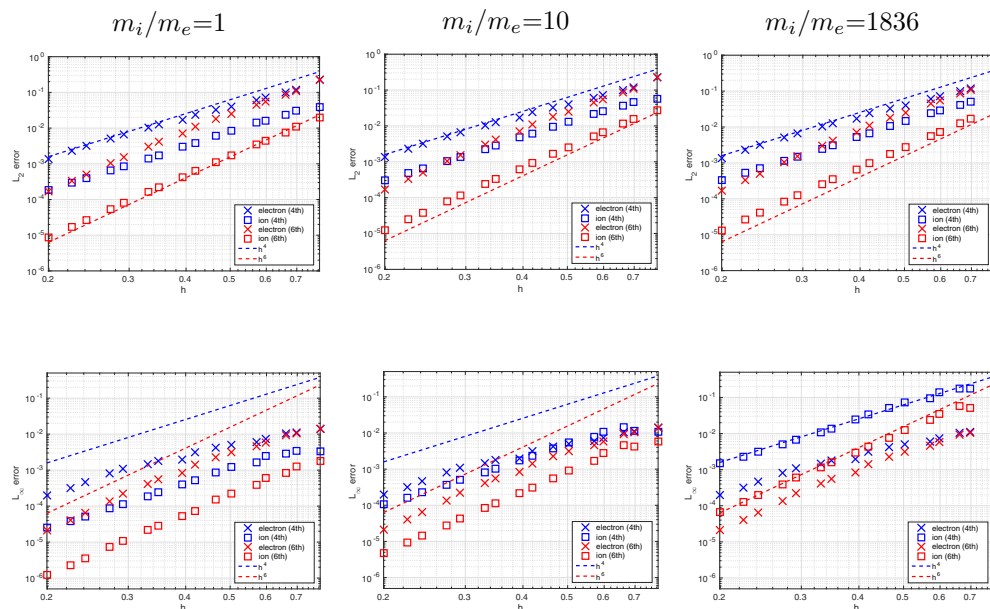
$m_i/m_e=1$ $m_i/m_e=10$ $m_i/m_e=1836$

FIG. 5. L_2- (top) and L_∞- (bottom) norm convergence for the manufactured solution, at fourth- and sixth-order accuracy and for increasing values of m_i/m_e. The reference lines are fixed for all cases so that trends with respect to mass ratio are more easily deduced.
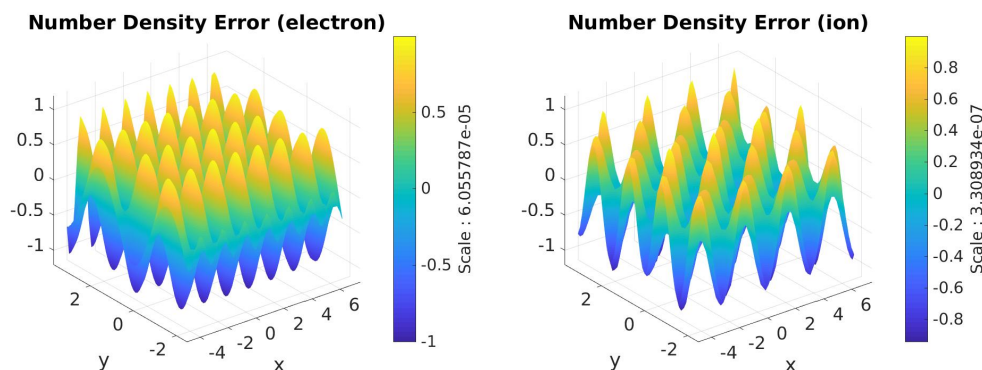

FIG. 6. Number density error for the manufactured electron (top) and ion (bottom) solutions, at sixth-order accuracy using 63 grid points in each direction. Note that the color scale for each figure has been normalized as indicated to the right of each color bar.

the case of the electron plasma, there appear to be no artifacts in the convergence behavior, and so one would expect the errors to be spatially smooth. Figure 6 shows the errors in the electron and ion charge density for the finest grid ($N_x = 63$) using the sixth-order scheme with $m_i/m_e = 1836$, where the smooth behavior of the error is clearly demonstrated.

4.2. Landau damping. Collisionless damping, usually referred to as Landau damping [35, 40], is an important feature of solutions to Vlasov–Poisson systems. Physically speaking, Landau damping is responsible for a variety of important phe-
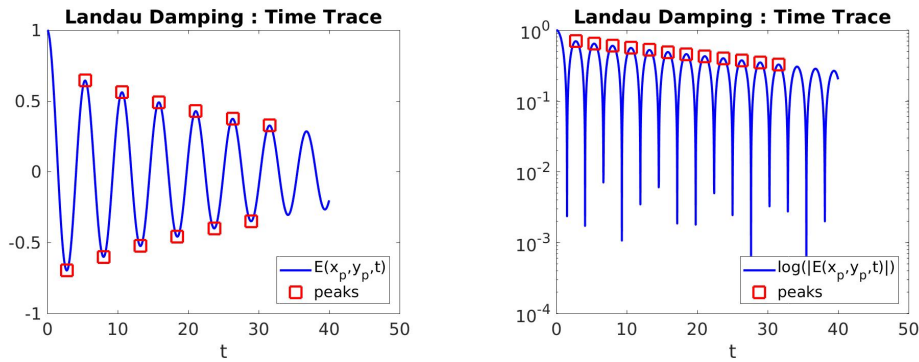
FIG. 7. *On the left is the time trace of the normalized electric field, and on the right is the log of the absolute value of that trace. Local minima and maxima of the field are indicated by red squares. The procedure for extracting these values, here called $E^{m,*}$, is described in the text. These extrema are used to extract decay rates and subsequently the frequency of the wave.*

nomena, e.g., setting thresholds for plasma instabilities [36], and effectively transferring wave energy to kinetic energy of resonant electrons or ions. As such, diagnosing Landau damping rates from numerical simulations is an important capability. Furthermore, the extraction of accurate decay or growth rates from simulation is one of the motivating drivers behind our use of continuum kinetic descriptions of plasmas, since their noiseless nature allows the observation of growth or decay over many decades. Therefore, it is important to investigate the accuracy of numerically extracted rates, and to assess any potential benefits in our use of high-order accurate numerical methods. Consider the classical tests from [33] of an initial value problem for a single species plasma with $m_e = 1$, $q_e = -1$, and initial conditions

$$(4.8) \qquad f_e(x, y, v_x, v_y, 0) = f_M(v_x, v_y; 1)\left(1 + \alpha \cos(k\lambda_D x)\right).$$

Here the wave number is set so $k\lambda_D = 1/3$ (λ_D stands for λ-Debye and $k\lambda_D$ is a physically relevant nondimensional parameter), and the domain taken to contain a single wave period in the x-direction by setting $L_x = 3\pi$. The transverse y-direction has no variation and so $L_y = 0.1$ is chosen to avoid the possibility of transverse instability growth [8]. Finally $\alpha = 10^{-6}$ so that the simulation remains essentially linear.[6] Note that because the simulation is essentially 1D+1V, the results presented here can be compared against results from other 1D+1V codes.

In this problem, the electric field is a standing wave which oscillates in time, and whose amplitude decays in time. One common way to diagnose this wave, is to extract a time trace of the electric field at a point in space. Because the problem is essentially linear, the exact location of the extraction is immaterial (provided the location is not a zero of the standing wave), and it is therefore convenient to normalize the time trace by the magnitude of the electric field at $t = 0$. Such a normalized time trace is illustrated in Figure 7, which also shows the log of the absolute value of the time trace. The apparent exponential decay in the time oscillating electric field corresponds to Landau, or collisionless, damping. Notice that in the figure the extrema in the field time trace are identified, since they will be used to extract a decay rate and oscillation frequency.

_____

[6]The nonlinearity in the Vlasov equation is essentially of quadratic type, and so this magnitude perturbation to the Maxwellian results in a nonlinearity entering on the relative order of 10^{-12}.

Unfortunately, the connection of Landau damping to the phase-space solutions of the Vlasov system is mathematically delicate, which leads to complications when diagnosing decay parameters from our, or indeed any other, numerical simulation. In particular, note that solutions to the Vlasov–Poisson system (2.1) are *dissipation free*, and indeed the equations are a reflection of a time-reversible Hamiltonian system with a nondiminishing energy. From the perspective of the PDEs then, one is led to the conclusion that there is no damping in the system. However, this conclusion stands in apparent contradiction to the observed exponential decay of field energy as illustrated in Figure 7. The resolution of this contradiction lies in the fact that the electric field is derived from the phase-space distribution using moment reduction. In a sense, the moment-reduced contribution of nondissipative modes leads to exponential decay of field energy. The difficulty in this dichotomy for the present discussion is that by using the initial conditions (4.8), one obtains a spectrum of decaying modes each with their own decay rate, the so-called Landau spectrum [29]. Determination of this Landau spectrum is a classical result from plasma physics, discussed, for example, in [29], and boils down to determining the complex roots, ω, of the kinetic dispersion relation

$$(4.9) \qquad 1 + \frac{1}{(k\lambda_D)^2} W\left(\frac{\omega}{k\lambda_D}\right) = 0.$$

In this dispersion relation the W-function, sometimes referred to as the dispersion function, is defined as

$$(4.10) \qquad W(z) = \frac{1}{\sqrt{2\pi}} \int_{\mathcal{C}} \frac{x}{x - z} \exp^{-\frac{x^2}{2}} = 1 + i\sqrt{\frac{\pi}{2}}\, z\, \mathrm{erfcx}\left(\frac{z}{\sqrt{2}}\right),$$

where $\mathcal{C}$ is the so-called Landau contour, and $\mathrm{erfcx}(z)$ is a scaled complimentary error function defined as

$$\mathrm{erfcx}(z) = e^{-z^2} \mathrm{erfc}(-iz).$$

The least damped solution ω_L is often referred to as the *Landau root*, and gives the asymptotic damping rate for the plasma oscillation, i.e., the Landau damping rate. Therefore, in order to observe Landau damping at a rate corresponding to the Landau root of (4.9), one would need to wait until such time as any contribution from more strongly damped modes have become negligible. The situation is further complicated in the present manuscript since our desire is to demonstrate sixth-order accurate convergence rates for extracted damping parameters. To show these rates, highly accurate answers are needed over a range of grid resolutions, but long-time simulations are problematic for coarse grids because of the well-known phenomenon of numerical recurrence [16].[7] Because of the subtleties in separately diagnosing the Landau root from the remaining Landau spectrum, we pursue a two-pronged approach. First, we choose to demonstrate the accuracy of the numerical approach for an average decay rate, which is derived from an electric field time trace, and is closely related to the damping parameters. To obtain an exact time trace, a pseudospectral discretization of the linearized equations is used, and convergence at the expected rates is demonstrated for both an electron plasma and a hydrogen plasma. Subsequently, for the case of an electron plasma, we return to the question of accurately identifying the Landau root from simulation, and compare those results to the Landau root as calculated using the kinetic dispersion relation (4.9).

---

[7]Note that numerical recurrence is in fact intimately tied to the dichotomy between the undamped phase-space spectrum, also called the van Kampen spectrum, and the Landau spectrum.

For the purposes of demonstrating numerical convergence behavior, an average decay rate and oscillation frequency are derived from the time trace of the electric field as follows. Consider the time trace $E(t)$, defined at a finite number of discrete time steps t_n for $t_n \in [0, T]$, each of which is denoted E^n.[8] Discrete local extrema in the data are identified by determining the values m such that $|E^m| > |E^{m \pm 1}|$. Note that the initial condition at $t = 0$ is not included in the list of discrete extrema since there are no data for $t < 0$. For each E^m, an eighth-order polynomial interpolant, $\tilde{E}(t)$, is fit through the data $E^{m \pm \ell}$ for $\ell = -4, -3, \ldots, 4$. The local extremum, $E^{m,*} = \tilde{E}(t^{m,*})$, is then found by seeking the local maximum (or minimum) of $\tilde{E}(t)$ for $t \in [t^{m-1}, t^{m+1}]$. For example, these points are indicated in Figure 7 with red squares. Given this set of local extrema, an average damping rate γ_A, is determined by seeking a least-squares fit line to the log of the data points $E^{m,*}$. Specifically, the decay rate is defined from the least-squares solution to the system

$$(4.11) \qquad c + \gamma_A t^{m,*} = \log |E^{m,*}|,$$

where c is a constant which is ignored. Having extracted an average damping rate γ_A, the average frequency of oscillation is determined as follows. First the time trace of the field is multiplied by the reciprocal of the extracted damping rate to eliminate the average exponential decay. The average frequency, ω_A is then determined from a least-squares fit to the system

$$(4.12a) \qquad \psi^n = E^n e^{\gamma_A t_n},$$
$$(4.12b) \qquad \psi^n = a_0 + a_1 \cos(\omega_A t_n) + b_1 \sin(\omega_A t_n),$$

where a_0, a_1, and b_1 are constants which are ignored.

Landau damping in electron plasma: Having described a procedure to extract an average damping rate and frequency from a time trace of the electric field, consider now an electron plasma with $m_e = 1$, $q_e = -1$, $\eta_e = 1$, and initial conditions to launch a standing plasma wave given by

$$(4.13) \qquad f(x, y, v_x, v_y, 0) = f_M(v_x, v_y; \eta_e) \left(1 + 10^{-6} \cos(k \lambda_D x)\right).$$

The problem is defined by $k \lambda_D = 1/3$ and the longitudinal domain is defined using $L_x = \pi / k \lambda_{D,e} = 3\pi$ to contain a single wave period. Because the problem is spatially one-dimensional, the transverse y-direction is taken to have a fixed number of grid points, $N_y = 7$, even as the grid is refined. So that the grid cells remain roughly square, the transverse length is defined using $L_y = \frac{N_y}{N_x} L_x$. The artificially truncated velocity boundaries are set using $v_{\max} = 7$ for all directions. A grid refinement study is performed using $N_x = N_\ell$, $N_{vx} = N_\ell$, $N_y = 7$, and $N_{vy} = 18$, where $N_\ell = 40 + 10\ell$ for $\ell \in [0, 10]$. Note that $N_{vy} = 18$ is chosen to be the number of points for which the discrete integration error $1 - \iint f_M dv_x dv_y$ is below machine precision. Finally, simulations are run to a final time of $t_f = 40$, and the final time in the data extraction process is taken to be $T = 32$.

To obtain an "exact" reference solution for the average damping rate and frequency, a separate pseudospectral discretization is used, and γ_A and ω_A are then extracted from the numerical solution. In particular, the 1D linearized Vlasov–Poisson system is first Fourier transformed in x to render all spatial derivatives as multiplication by $ik\lambda_D$. A very fine velocity space grid with 32768 points is then used to obtain

---

[8] In the present work we have assumed that the velocity grid is fine enough to exclude numerical recurrence before the final time T.
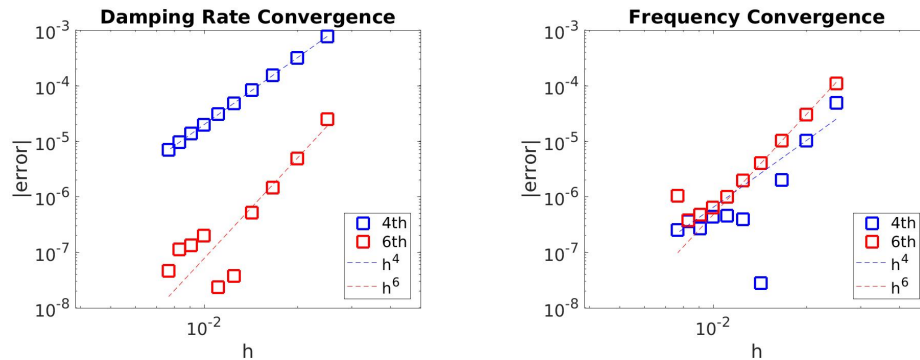
FIG. 8. *Error in the extracted average damping rate γ_A and frequency ω_A for an electron plasma. Reference lines indicating $\mathcal{O}(h^4)$ and $\mathcal{O}(h^6)$ are also included, and the average convergence behavior is observed to be near the designed rate.*

a large system of ODEs. Finally, the RK-6 integrator is used to generate a time trace of the electric field. The average decay rate and frequency are then found to be[9]

$$(4.14) \qquad \gamma_A = -2.610715 \times 10^{-2}, \qquad \omega_A = 1.200418.$$

The convergence behavior of the LOKI results to these reference values is presented in Figure 8, which shows the error in the average damping rate and frequency. These results indicate that the average observed convergence rates are at or near the expected values of 4 or 6, although from one grid to the next there is at times significant variability in this rate. In this case, it is interesting to note that the error in the damping rate is approximately 2 orders of magnitude smaller for the sixth-order code than for the fourth-order code for all grids. However, for the frequency the story is reversed with the fourth-order result being marginally more accurate for all grid resolutions. This is a counterintuitive result, and may be related to a sign change in the error in ω_A for the fourth-order code near $N_\ell = 70$. This appears to be purely fortuitous in this case, and superior behavior for the fourth-order code is not observed in any other case or quantity of interest. Note also that since the scheme is exactly mass conservative by construction, one would also expect momentum conservation (due to linearity). However, other moments of the distribution function (e.g., total energy) may not be exactly conserved. Nevertheless, in this case we observe conservation of f, x- and y-momenta, and the total energy (kinetic plus electrostatic potential) to machine precision. The latter is due to the fact that a small initial perturbation is used to ensure Landau damping in the linear regime. Therefore, diagnosing convergence of the total energy, as was done for example in [13], is not viable here.

The previous analysis effectively demonstrates that the numerical solution of the IVP is converging to the exact solution of the IVP at the expected rate. From a physical perspective it is important to make contact with the theoretical damping rate and frequency associated with the Landau root of the kinetic dispersion relation (4.9). As discussed previously, the presence of a spectrum of decaying modes with a variety of decay rates led us to consider the average quantities γ_A and ω_A. However by waiting long enough, the initial transients associated with modes decaying at higher

---

[9]These values appear to have at least 7 correct digits since they agree with results from coarser grids.
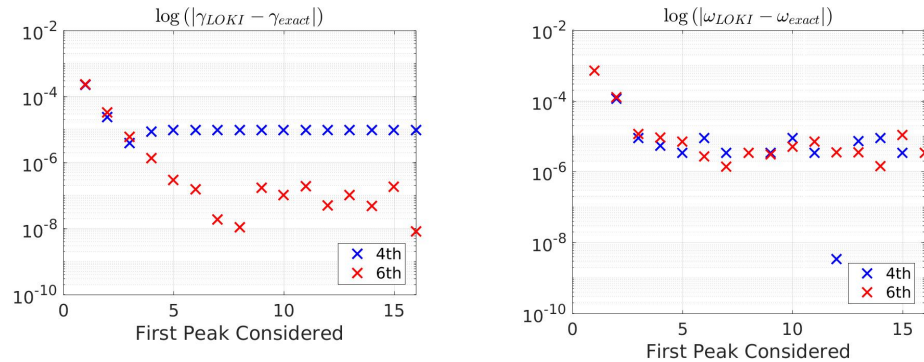
FIG. 9. *Comparison of the average damping rate for the single species plasma using $N_\ell = 140$ over successively later time intervals as indicated by the first electric field peak which is considered. The exact value here is derived from the kinetic dispersion relation* (4.9).

rates than that associated with the Landau root will become negligible. To observe this phenomenon, simulation results on the finest grid with $N_\ell = 140$ are extended to a final time of $t_f = 100$. Note that this final time is significantly less than the recurrence time for this grid resolution. The average damping rate over 12 peaks[10] in the electric field time trace is then computed for successively later time intervals. That is to say, the rate is computed over peaks 1–12, then over peaks 2–13, and so on. These results are shown in Figure 9 for both the fourth- and sixth-order accurate schemes. For reference, the Landau root of the kinetic dispersion relation has $\gamma = -2.587368 \times 10^{-2}$ and $\omega = 1.200109$. Both the damping rate and frequency are seen to converge toward the Landau root as a function of the first peak which is considered. However, the accuracy of the simulation results in this comparison is fixed (since the grid is fixed), and the level of error saturation observed in Figure 9 will therefore be a reliable indicator of numerical error in the simulation. This is in agreement with the results in Figure 8 for the finest computations.

Landau damping in two-species plasma: We move now to Landau damping in a two-species plasma corresponding to hydrogen with $m_e = 1$, $q_e = -1$, $\eta_e = 1$ for the electrons, and $m_i = 1836$, $q_i = 1$, $T_i = 1/8$, and $\eta_i = \sqrt{m_i/T_i}$ for the ions. The plasma wave is launched from initial conditions

$$f_e(x, y, v_x, v_y, 0) = f_{M,e}(v_x, v_y; \eta_e) \left(1 + 10^{-6} \cos(k\lambda_D x)\right), \tag{4.15a}$$

$$f_i(x, y, , v_x, v_y, 0) = f_{M,i}(v_x, v_y; \eta_i). \tag{4.15b}$$

The inclusion of an additional kinetic species allows for multiple kinds of plasma oscillations, the principal ones being the EPW and the IAW [44]. The EPW frequency, $\omega_{pe} = \sqrt{4\pi N_e e^2/m_e}$, and its Landau damping rate, γ_L (proportional to ω_{pe}) are much larger than the IAW frequency, $\omega_{iaw} = k\sqrt{T_e/m_i}$, and Landau damping rate, γ_{iaw} (proportional to ω_{iaw}). The ratio of these frequencies is proportional to the square root of the mass ratio, $\omega_{iaw}/\omega_{pe} = k\lambda_{de}\sqrt{m_e/m_i}$. Note that $k\lambda_{de} < 1$ for resonant plasma oscillation. We would therefore expect the Landau spectrum to have two distinct families of decay rates, the first associated with decay of an EPW with mobile ions and the second associated with decay of the IAW, and the time-scale separation between these two dynamics will scale with the square root of the mass

---

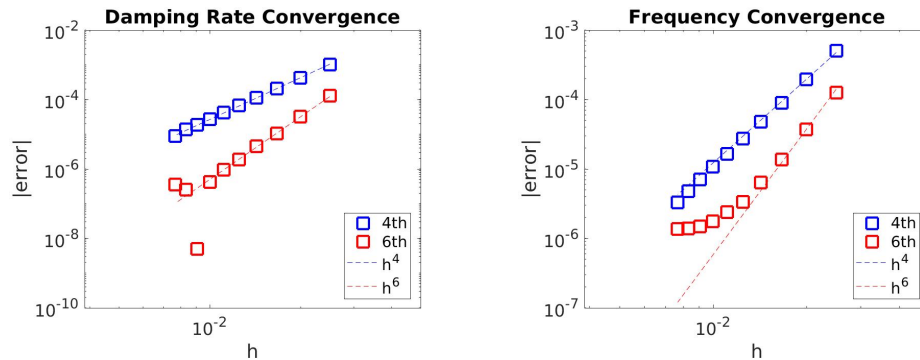[10]This is the number of peaks used in the results presented in Figure 8.

FIG. 10. *Error in the extracted average damping rate γ_A and frequency ω_A for a hydrogen plasma. Reference lines indicating $\mathcal{O}(h^4)$ and $\mathcal{O}(h^6)$ are also included, and the average convergence behavior is observed to be near the designed rate.*

ratio. Thus one would expect that for early times EPW decay is observed, but that only on much longer time scales (on the order of 40x longer in this case) could one observe IAW decay. We therefore anticipate that this study diagnoses primarily EPW decay, and there is no attempt to make contact with the Landau spectrum since this is computationally prohibitive. Here we take $k\lambda_D = 0.4$, $L_x = \pi/k\lambda_D$, $L_y = \frac{N_y}{N_x}L_x$. The artificial velocity boundaries are taken to be defined by $v_{max,e} = 7$, $v_{max,i} = 10/\eta$. Similarly to the case of an electron plasma above, a grid refinement study is conducted with $N_x = N_\ell$, $N_y = 7$, $N_{vx} = N_\ell$, and $N_{vy} = 18$ with $\ell \in [0, 9]$. For this case, the pseudospectral discretization of the 1D linearized Vlasov–Poisson system yields the exact reference solution

$$(4.16) \qquad \gamma = -6.630239 \times 10^{-2}, \qquad \omega = 1.285323.$$

The convergence behavior of the LOKI results to these reference values is presented in Figure 10, which shows the error in the average damping rate and frequency. These results indicate very clean convergence rates at or near the expected values of 4 or 6, respectively. Even here, however, the frequency is seen to be saturating at roughly 10^{-6}, which may be the result of errors in comparing the solution to the nonlinear equations from LOKI to solutions from the the linearized pseudospectral code. Importantly, unlike the case of an EPW above, all cases here show that the sixth-order scheme yields not only asymptotically faster convergence rates, but that the error at a given resolution is orders of magnitude smaller than for the results from the fourth-order scheme. Note also that as in the case of a single species, we observe conservation of f, x- and y-momenta, and the total energy (kinetic plus electrostatic potential) to machine precision for these cases.

4.3. Instability of IAWs. We now discuss potential practical benefits of high-order accurate schemes, and discuss simulation results for a particular physics case obtained from the fourth- and sixth-order schemes. For this purpose, we choose a case of general physical interest, namely that of the decay of an IAW. The principal result demonstrated here is a reduction by a factor of ≈ 40 in the total number of space-time grid points, and a factor of ≈ 16 in computational cost required to obtain a measurement of interest when comparing the sixth- and fourth-order runs.

The system under consideration is doubly periodic in configuration space, and the plasma wave is excited using a monochromatic sinusoidal electric field $E_D(x, t) =$
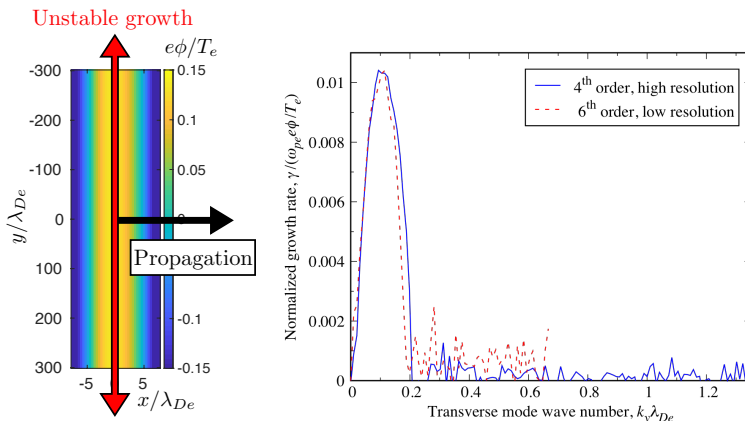
FIG. 11. *Diagram showing filamentary growth behavior and a measurement of the unstable transverse mode growth rates, γ, versus transverse wave number for fourth- and sixth-order simulations, where the number of space-time grid points for the sixth-order run is reduced by a factor of $2.44 \times 2^4 \approx 40$ relative to the fourth-order run.*

$E_0(t)\sin(k_D x - \omega_D t)$, where $E_0(t)$ is a temporal envelope. The driver frequency, ω_D, and wave number, k_D, are chosen satisfying the IAW dispersion relation, leading to near-resonant excitation of an IAW (see, e.g., the discussion in [9]). The system length along x is set to be equal to the wavelength of the IAW, while the width along y is chosen much greater. At a specified time the driver is turned off, and the excited IAW is allowed to propagate freely until a filamentary instability develops (longitudinal instability is not possible, since modes with $k_x < k_D$ cannot be represented in the chosen system). Spatial Fourier analysis reveals transverse decay modes that grow exponentially in time, with growth rate $\gamma = \gamma(k_D, k_y)$, until the decay mode amplitudes become large in comparison to the primary mode, and the mother IAW collapses. A simple diagram of the linear stage of this process is provided in Figure 11 (left). The existence of γ and its functional dependence on k_y is of interest to basic plasma physics and has been the subject of numerous theoretical and numerical studies [46, 19, 15], as well as dedicated laboratory experiments [45]. The growth rate γ is the primary measurement used here to compare the outcome, and related computational cost, from simulations at fourth and sixth order.

The two-species plasma is defined using $m_e = 1$, $q_e = -1$, $\eta_e = 1$ for the electrons, and $m_i = 1836$, $q_i = 1$, $T_i = 1/8$, and $\eta_i = \sqrt{m_i/T_i}$ for the ions. The spatial wave number of the driver is set to be $k_D = 0.4$ with corresponding near-resonant frequency $\omega_D = 0.0108$. The driver is applied for $t < 1000$ with an amplitude 0.0125.[11] The physical domain is defined using $L_x = \pi/k_D$, $L_y = 96\pi$, $v_{x,\max,e} = v_{y,\max,e} = 7$, $v_{x,\max,i} = 0.0825$, $v_{y,\max,i} = 0.0578$. For the fourth-order simulation, we use $N_x = 40$, $N_y = 256$, $N_{vx,e} = N_{vx,i} = 128$, and $N_{vy,e} = N_{vy,i} = 96$. For the sixth-order simulation the grid resolution is cut in half giving $N_x = 20$, $N_y = 128$, $N_{vx,e} = N_{vx,i} = 64$, $N_{vy,e} = N_{vy,i} = 48$. As a result of this reduction in resolution, the time step for $\Lambda = 0.95$ is a factor of 2.44 larger for the sixth-order run in comparison to the fourth-order run. Accordingly, the total number of space-time grid points for the sixth-

---

[11]Note that the driver is turned on and off smoothly so that particle trapping is adiabatic; see [4, 15] for details.

order run is reduced by a factor of $2.44 \times 2^4 \approx 40$ when compared to the fourth-order run. We note that if semi-Lagrangian or implicit methods were used, the time step could be chosen arbitrarily large from the perspective of stability. However, accurately capturing the IAW dynamics of interest requires resolving the (comparatively fast) electron dynamics; accordingly, the time step must resolve oscillations of period $\tau_{pe} = 2\pi/\omega_{pe}$. Requiring 20 points per period (mimicking the chosen spatial resolution of a wave length at sixth order in this case) sets a maximum time step of $\Delta t = \tau_{pe}/20 \approx 0.31$. At sixth order, the time step selected by the LOKI code for this problem is $\Delta t \approx 0.088$. Thus, a method without any time-step restriction based on stability would offer only a modest increase in the time step, and any potential improvement in computational cost may be negated by additional overhead inherent in such methods. It is also useful to note that the fourth-order case used 4096 CPUs, while the sixth-order case used only 256 CPUs.[12] Nevertheless, to reach a given simulation time t, the required wall clock times were approximately equal (in fact the sixth-order case completed in 10% less wall time, although this difference is very likely within run-to-run variability in machine performance).

Measured values of γ versus all represented k_y are shown in Figure 11 (right) for the fourth- and sixth-order simulations, extracted during the linear phase of transverse mode growth. γ has been normalized to the instantaneous wave amplitude to suppress small variations in instantaneous ϕ from complicating the comparison (for this regime of parameters, γ is approximately proportional to ϕ [15]).[13] Measurements from both simulations agree to within the accuracy of the fit to the unstable mode amplitudes for which R^2 values are in the range $[0.7-0.95]$. After the driver is turned off and until the end of the measurement (a duration of $\sim 2 \times 10^4$), energy is conserved in the fourth-order case to within 3%, while energy is conserved in the sixth-order case to within 0.5%. Results obtained using the fourth-order accurate scheme, but with the coarser grid resolution show significant unphysical nonlinearity in the early evolution of the unstable modes (i.e., deviation from exponential growth), and energy conservation only to within 15% over the same duration. Note also that in this example, the change from fourth- to sixth-order accuracy offers a practical reduction of ≈ 40 in the total number of space-time grid points, and a factor of ≈ 16 in computational cost. However, it is quite probable that different physical scenarios or different measurements could exhibit a greater improvement in performance. In this case, the available gains are likely limited by a minimum resolution in velocity space required to resolve the bounce motion of particles trapped in the wave potential [9, 15].

5. Conclusions. In this work, we have described a general framework for high-order-accurate simulation of Vlasov equations. The algorithms use conservative FDs, expressed as a difference of fluxes, and so the algorithms are trivially exactly conservative. In the present work, both fourth- and sixth-order accurate schemes are described in detail. Nonlinear BWENO limiting is used to introduce minimal stabilizing dissipation, needed for underrepresented solution features, but the dissipation vanishes in well-represented regions. Using minimal dissipation is critical for long-time simulation, where artificial diffusion would tend to damp the approximation toward zero.

---

[12]CPU counts are for the Quartz machine at LLNL which has Intel Xeon E5-2695 cores and an Omni-Path interconnect.

[13]Note that both the observed distribution function and the extracted growth rates imply that even at late time the solution remains largely smooth on the grid. In fact the BWENO limiter has had significant effect only in isolated regions in space and time where the distribution function appears "rough" on the grid.

Detailed results of code verification studies using the presented algorithms is pursued using the MMS. As is typical for manufactured solution verification, source terms are added to the governing equations so that the solution to the modified system is known, and convergence studies can therefore be pursued. For the Vlasov–Poisson system under study, exact manufactured solutions are taken to be spatially sinusoidal perturbations of Maxwellian distributions, with the result that source terms are only required for the Vlasov equation itself. This greatly simplifies the implementation, and therefore lowers the barrier of entry to detailed code verification for us and other research groups. Using this procedure, the expected fourth- and sixth-order accurate convergence is demonstrated for both an electron plasma, and a series of electron-ion plasmas including cases with a physically realistic mass ratio corresponding to hydrogen. Having verified the expected convergence rate of the code, we moved on to results concerning Landau damping. Owing to the presence of a spectrum of decaying modes in the Landau spectrum, we show asymptotic convergence rates for an extracted average damping rate and oscillation frequency. In the case of an electron plasma, we also pursue a rigorous identification of the Landau root itself, by considering successively later times so that the presence of more strongly damped modes become negligible. Finally, we discuss the growth of transverse instability in an IAW, and show that the higher-order schemes offer significant practical cost savings when considering the extraction of linear growth rates.

There is a wide variety of avenues for potential future work in this area. From the perspective of the discretization, the efficiency of even higher-order accurate discretizations, particularly for practically realizable numbers of grid points, would be quite interesting. Similarly, the possibility of extending the highly efficient algorithms described here to fully 6D phase space is enticing. There are also many possibilities for future work that involve relaxing basic assumptions of the models. For example, moving from electrostatics to the full equations of electromagnetism, or the inclusion of relativistic effects are both conceptually straightforward exercises that would significantly widen the set of physical scenarios that could be considered.

<div align="center">REFERENCES</div>

[1] J. B. Angel, J. W. Banks, and W. D. Henshaw, *High-order upwind schemes for the wave equation on overlapping grids: Maxwell's equations in second-order form*, J. Comput. Phys., 352 (2018), pp. 534–567.

[2] T. D. Arber and R. G. L. Vann, *A critical comparison of Eulerian-grid-based Vlasov solvers*, J. Comput. Phys., 180 (2002), pp. 339–357.

[3] U. M. Ascher and L. R. Petzold, *Computer Methods for Ordinary Differential Equations and Differential-Algebraic Equations*, SIAM, Philadelphia, 1998.

[4] J. W. Banks, R. L. Berger, S. Brunner, B. I. Cohen, and J. A. F. Hittinger, *Two-dimensional Vlasov simulation of electron plasma wave trapping, wavefront bowing, self-focusing, and sideloss*, Phys. Plasmas, 18 (2011), 052102.

[5] J. W. Banks, S. Brunner, R. L. Berger, and T. M. Tran, *Vlasov simulations of electron-ion collision effects on damping of electron plasma waves*, Phys. Plasmas, 23 (2016), 032108.

[6] J. W. Banks and W. D. Henshaw, *Upwind schemes for the wave equation in second-order form*, J. Comput. Phys., 231 (2012), pp. 5854–5889.

[7] J. W. Banks and J. A. F. Hittinger, *A new class of non-linear, finite-volume methods for Vlasov simulation*, IEEE Trans. Plasma. Sci., 38 (2010), pp. 2198–2207.

[8] R. L. Berger, S. Brunner, J. W. Banks, B. I. Cohen, and B. J. Winjum, *Multi-dimensional Vlasov simulations and modeling of trapped-electron-driven filamentation of electron plasma waves*, Phys. Plasmas, 22 (2015), 055703.

[9] R. L. Berger, S. Brunner, T. Chapman, L. Divol, C. H. Still, and E. J. Valeo, *Electron and ion kinetic effects on non-linearly driven electron plasma and ion acoustic waves*, Phys. Plasmas, 20 (2013), 032107.

[10] N. BESSE AND E. SONNENDRÜCKER, *Semi-Lagrangian schemes for the Vlasov equation on an unstructured mesh of phase space*, J. Comput. Phys., 191 (2003), pp. 341–376.

[11] D. L. BROWN, *private communication*, 1987.

[12] J. CANDY AND R. E. WALTZ, *An Eulerian gyrokinetic-Maxwell solver*, J. Comput. Phys., 182 (2003), pp. 545–581.

[13] F. CASAS, N. CROUSEILLES, E. FAOU, AND M. MEHRENBERGER, *High-order Hamiltonian splitting for the Vlasov–Poisson equations*, Numer. Math., 135 (2017), pp. 769–801.

[14] J. CASPER AND H. L. ATKINS, *A finite-volume high-order ENO scheme for two-dimensional hyperbolic systems*, J. Comput. Phys., 106 (1993), pp. 62–76.

[15] T. CHAPMAN, R. L. BERGER, B. I. COHEN, J. W. BANKS, AND S. BRUNNER, *Longitudinal and transverse instability of ion acoustic waves*, Phys. Rev. Lett., 119 (2017), 055002.

[16] C. Z. CHENG AND G. KNORR, *The integration of the Vlasov equation in configuration space*, J. Comput. Phys., 22 (1976), pp. 330–351.

[17] Y. CHENG, A. J. CHRISTLIEB, AND X. ZHONG, *Energy-conserving discontinuous Galerkin methods for the Vlasov-Maxwell system*, J. Comput. Phys., 279 (2014), pp. 145–173.

[18] G. S. CHESSHIRE AND W. D. HENSHAW, *Composite overlapping meshes for the solution of partial differential equations*, J. Comput. Phys., 90 (1990), pp. 1–64.

[19] B. I. COHEN, E. A. WILLIAMS, R. L. BERGER, D. PESME, AND C. RICONDA, *Stimulated Brillouin backscattering and ion acoustic wave secondary instability*, Phys. Plasmas, 16 (2009), 032701.

[20] P. COLELLA, M. DORR, J. HITTINGER, AND D. MARTIN, *High-order, finite-volume methods in mapped coordinates*, J. Comput. Phys., 230 (2011), pp. 2952–2976.

[21] W. DORLAND, F. JENKO, M. KOTSCHENREUTHER, AND B. N. ROGERS, *Electron temperature gradient turbulence*, Phys. Rev. Lett., 85 (2000), pp. 5579–5582.

[22] E. ESAREY, C. B. SCHROEDER, AND W. P. LEEMANS, *Physics of laser-driven plasma-based electron accelerators*, Rev. Mod. Phys., 81 (2009), pp. 1229–1285.

[23] F. FILBET AND E. SONNENDRÜCKER, *Comparison of Eulerian Vlasov solvers*, Comput. Phys. Commun., 150 (2003), pp. 247–266.

[24] F. FILBET, E. SONNENDRÜCKER, AND P. BERTRAND, *Conservative numerical schemes for the Vlasov equation*, J. Comput. Phys., 172 (2001), pp. 166–187.

[25] W. GROPP, E. LUSK, AND R. THAKUR, *Using MPI-2: Advanced Features of the Message-Passing Interface*, MIT Press, Cambridge, MA, 1999.

[26] M. GUTNIC, M. HAEFELE, I. PAUN, AND E. SONNENDRÜCKER, *Vlasov simulations on an adaptive phase space mesh*, Comput. Phys. Commun., 164 (2004), pp. 214–219.

[27] A. K. HENRICK, T. D. ASLAM, AND J. M. POWERS, *Mapped weighted essentially non-oscillatory schemes: Achieving optimal order near critical points*, J. Comput. Phys., 207 (2005), pp. 542–567.

[28] W. D. HENSHAW AND G. CHESSHIRE, *Multigrid on composite meshes*, SIAM J. Sci. Comput., 8 (1987), pp. 914–923.

[29] S. ICHIMARU, *Basic Principles of Plasma Physics: A Statistical Approach*, W. A. Benjamin, London, 1973.

[30] G.-S. JIANG AND C.-W. SHU, *Efficient implementation of weighted ENO schemes*, J. Comput. Phys., 126 (1996), pp. 202–228.

[31] O. KLIMO, J. PSIKAL, J. LIMPOUCH, AND V. T. TIKHONCHUK, *Monoenergetic ion beams from ultrathin foils irradiated by ultrahigh-contrast circularly polarized laser pulses*, Phys. Rev. ST Accel. Beams, 11 (2008), 031301.

[32] M. KOTSCHENREUTHER, G. REWOLDT, AND W. M. TANG, *Comparison of initial value and eigenvalue codes for kinetic toroidal plasma instabilities*, Comput. Phys. Commun., 88 (1995), pp. 128–149.

[33] N. A. KRALL AND A. W. TRIVELPIECE, *Principles of Plasma Physics*, McGraw-Hill, New York, 1973.

[34] A. KURGANOV AND S. TSYNKOV, *On Spectral Accuracy of Quadrature Formulae Based on Piecewise Polynomial Interpolation*, Technical report, CRSC-TR07-11, North Carolina State University, Raleigh, NC, 2007.

[35] L. D. LANDAU, *On the vibration of the electronic plasma*, J. Phys. (USSR), 10 (1946), pp. 25–34.

[36] J. D. LINDL, P. AMENDT, R. L. BERGER, S. G. GLENDINNING, S. H. GLENZER, S. W. HAAN, R. L. KAUFFMAN, O. L. LANDEN, AND L. J. SUTER, *The physics basis for ignition using indirect-drive targets on the National Ignition Facility*, Phys. Plasmas, 11 (2004), pp. 339–491.

[37] J. LUO, M. CHEN, W. Y. WU, S. M. WENG, Z. M. SHENG, C. B. SCHROEDER, D. A. JAROSZYNSKI, E. ESAREY, W. P. LEEMANS, W. B. MORI, AND J. ZHANG, *Multistage coupling of*

laser-wakefield accelerators with curved plasma channels, Phys. Rev. Lett., 120 (2018), 154801.

[38] V. M. MALKIN, G. SHVETS, AND N. J. FISCH, *Fast compression of laser beams to highly overcritical powers*, Phys. Rev. Lett., 82 (1999), pp. 4448–4451.

[39] S. F. MARTINS, R. A. FONSECA, W. LU, W. B. MORI, AND L. O. SILVA, *Exploring laser-wakefield-accelerator regimes for near-term lasers using particle-in-cell simulation in Lorentz-boosted frames*, Nature Phys., 6 (2010), pp. 311–316.

[40] C. MOUHOT AND C. VILLANI, *On Landau damping*, Acta Math., 207 (2011), pp. 29–201.

[41] G. MOUROU AND T. TAJIMA, *More intense, shorter pulses*, Science, 331 (2011), pp. 41–42.

[42] T. NAKAMURA, R. TANAKA, T. YABE, AND K. TAKIZAWA, *Exactly conservative semi-Lagrangian scheme for multi-dimensional hyperbolic equations with directional splitting technique*, J. Comput. Phys., 174 (2001), pp. 171–207.

[43] T. NAKAMURA AND T. YABE, *Cubic interpolated propagation scheme for solving the hyperdimensional Vlasov-Poisson equation in phase space*, Comput. Phys. Commun., 120 (1999), pp. 122–154.

[44] D. P. NICHOLSON, *Introduction to Plasma Theory*, Wiley, New York, 1983.

[45] C. NIEMANN, S. H. GLENZER, J. KNIGHT, L. DIVOL, E. A. WILLIAMS, G. GREGORI, B. I. COHEN, C. CONSTANTIN, D. H. FROULA, D. S. MONTGOMERY, AND R. P. JOHNSON, *Observation of the parametric two-ion decay instability with Thomson scattering*, Phys. Rev. Lett., 93 (2004), 045004.

[46] D. PESME, C. RICONDA, AND V. T. TIKHONCHUK, *Parametric instability of a driven ion-acoustic wave*, Phys. Plasmas, 12 (2005), 092101.

[47] D. QUINLAN, *A++/P++ Class Libraries*, Research report, LA-UR-95-3273, Los Alamos National Laboratory, Los Alamos, NM, 1995.

[48] P. J. ROACHE, *Code verification by the method of manufactured solutions*, ASME J. Fluids Eng., 124 (2002), pp. 4–10.

[49] C.-W. SHU, *Essentially Non-oscillatory and Weighted Essentially Non-oscillatory Schemes for Hyperbolic Conservation Laws*, Technical report, NASA-CR-97-206253, NASA Langley Research Center, Hampton, VA, 1997.

[50] C.-W. SHU, *Essentially non-oscillatory and weighted essentially non-oscillatory schemes for hyperbolic conservation laws*, in Advanced Numerical Approximation of Nonlinear Hyperbolic Equations, A. Quarteroni, ed., Lecture Notes in Math. 1697, Springer, New York, 1998, pp. 325–432.

[51] D. A. SILANTYEV, P. M. LUSHNIKOV, AND H. A. ROSE, *Langmuir wave filamentation in the kinetic regime. I. Filamentation instability of Bernstein-Greene-Kruskal modes in multidimensional Vlasov simulations*, Phys. Plasmas, 24 (2017), 042104.

[52] D. A. SILANTYEV, P. M. LUSHNIKOV, AND H. A. ROSE, *Langmuir wave filamentation in the kinetic regime. II. Weak and strong pumping of nonlinear electron plasma waves as the route to filamentation*, Phys. Plasmas, 24 (2017), 042105.

[53] N. J. SIRCOMBE AND T. D. ARBER, *VALIS: A split-conservative scheme for the relativistic 2D Vlasov-Maxwell system*, J. Comput. Phys., 228 (2009), pp. 4773–4788.

[54] D. STRICKLAND AND G. MOUROU, *Compression of amplified chirped optical pulses*, Optics Commun., 56 (1985), pp. 219–221.

[55] L. N. TREFETHEN AND J. A. C. WEIDEMAN, *The exponentially convergent trapezoidal rule*, SIAM Rev., 56 (2014), pp. 385–458.

[56] G. V. VOGMAN, U. SHUMLAK, AND P. COLELLA, *Conservative fourth-order finite-volume Vlasov-Poisson solver for axisymmetric plasmas in cylindrical (r,vr,vz) phase space coordinates*, J. Comput. Phys., 373 (2018), pp. 877–899.

[57] R. WANG AND R. S. SPITERI, *Linear instability of the fifth-order WENO method*, SIAM J. Numer. Anal., 45 (2007), pp. 1871–1901.

[58] S. WEBER, C. RICONDA, L. LANCIA, J.-R. MARQUÈS, G. A. MOUROU, AND J. FUCHS, *Amplification of ultrashort laser pulses by Brillouin backscattering in plasmas*, Phys. Rev. Lett., 111 (2013), 055004.

[59] B. J. WINJUM, R. L. BERGER, T. CHAPMAN, J. W. BANKS, AND S. BRUNNER, *Kinetic simulations of the self focusing and dissipation of finite-width electron plasma waves*, Phys. Rev. Lett., 111 (2013), 105002.

[60] L. YIN, B. J. ALBRIGHT, K. J. BOWERS, D. JUNG, J. C. FERNÁNDEZ, AND B. M. HEGELICH, *Three-dimensional dynamics of breakout afterburner ion acceleration using high-contrast short-pulse laser and nanoscale targets*, Phys. Rev. Lett., 107 (2011), 045003.